The Astronomical Journal, 156:179 (16pp), 2018 October
https://doi.org/10.3847/1538-3881/aadd9c

Kinematics of Highly *r*-process-enhanced Field Stars: Evidence for an Accretion Origin and Detection of Several Groups from Disrupted Satellites

Ian U. Roederer[1,2], Kohei Hattori[1], and Monica Valluri[1]
[1] Department of Astronomy, University of Michigan, 1085 S. University Ave., Ann Arbor, MI 48109, USA; iur@umich.edu
[2] Joint Institute for Nuclear Astrophysics—Center for the Evolution of the Elements (JINA-CEE), USA
Received 2018 June 26; revised 2018 August 23; accepted 2018 August 27; published 2018 October 4

Abstract

We present the kinematics of 35 highly *r*-process-enhanced ($[\mathrm{Eu/Fe}] \geqslant +0.7$) metal-poor ($-3.8 < [\mathrm{Fe/H}] < -1.4$) field stars. We calculate six-dimensional positions and velocities, evaluate energies and integrals of motion, and compute orbits for each of these stars using parallaxes and proper motions from the second *Gaia* data release and published radial velocities. All of these stars have halo kinematics. Most stars (66%) remain in the inner regions of the halo (<13 kpc), and many (51%) have orbits that pass within 2.6 kpc of the Galactic center. Several stars (20%) have orbits that extend beyond 20 kpc, including one with an orbital apocenter larger than the Milky Way virial radius. We apply three clustering methods to search for structure in phase space, and we identify eight groups. No abundances are considered in the clustering process, but the [Fe/H] dispersions of the groups are smaller than would be expected by random chance. The orbital properties, clustering in phase space and metallicity, and the lack of highly *r*-process-enhanced stars on disk-like orbits, indicate that such stars likely were accreted from disrupted satellites. Comparison with the galaxy luminosity–metallicity relation suggests $M_V \gtrsim -9$ for most of the progenitor satellites, characteristic of ultra-faint or low-luminosity classical dwarf spheroidal galaxies. Environments with low rates of star formation and Fe production, rather than the nature of the *r*-process site, may be key to obtaining the [Eu/Fe] ratios found in highly *r*-process-enhanced stars.

Key words: galaxies: dwarf – Galaxy: halo – stars: abundances – stars: kinematics and dynamics – stars: Population II

1. Introduction

The heaviest elements found in many metal-poor stars were produced by the rapid neutron-capture process (*r*-process) in earlier generations of stars. Work by Gilroy et al. (1988) demonstrated that genuine differences exist in the overall levels of enhancement of *r*-process elements relative to Fe in metal-poor stars. The recognition of the highly *r*-process-enhanced star CS 22892-052 by Sneden et al. (1994) in the HK Survey of Beers et al. (1992) erased any lingering doubt about the inhomogeneous distribution of *r*-process elements in the environments where metal-poor stars formed. Stars that exhibit Eu/Fe ratios at least 10 times higher than in the Sun, like CS 22892-052, comprise only a small fraction (≈3%; Barklem et al. 2005) of all metal-poor field stars, and none are known to be physically associated with each other (Roederer 2009).

The environmental impact of the *r*-process—expressed through the occurrence frequency, distribution, and enhancement levels of *r*-process elements in stars—can help associate *r*-process abundance patterns with their nucleosynthetic origins. Observations of the kilonova associated with gravitational wave event GW170817 (Abbott et al. 2017a, 2017b) provide the most direct confirmation that neutron-star mergers are a site capable of producing heavy elements by *r*-process nucleosynthesis (e.g., Cowperthwaite et al. 2017; Drout et al. 2017; Kasen et al. 2017; Tanvir et al. 2017). The occurrence frequency and level of *r*-process enhancement of stars in dwarf galaxies supports this conclusion (e.g., Ji et al. 2016a; Safarzadeh & Scannapieco 2017; Tsujimoto et al. 2017), although those results alone cannot exclude rare classes of supernovae as an additional site (e.g., Tsujimoto & Nishimura 2015; Beniamini et al. 2016). Chemical evolution models (Côté et al. 2018) and simulations (Naiman et al. 2018) can help generalize this result to *r*-process production in the Milky Way. The ^{244}Pu abundance in deep-sea sediments, which can be used to infer the content of this *r*-process-only isotope in the ISM, also points to rare *r*-process events like neutron-star mergers (Hotokezaka et al. 2015; Wallner et al. 2015).

We lack similar, direct knowledge of the birth environments of highly *r*-process-enhanced stars in the Milky Way halo field. An increasing number of these stars are now known (e.g., Hansen et al. 2018, and other ongoing work by the *R*-Process Alliance). Their proximity to the Sun permits detailed abundance inventories to be derived from optical, ultraviolet, and near-infrared spectra (e.g., Sneden et al. 1998; Roederer et al. 2012b; Afşar et al. 2016). Five-parameter astrometric solutions (parallax, R.A., decl., proper motion in R.A., proper motion in decl.) are now available for many of these stars in the second data release of the *Gaia* mission (DR2; Lindegren et al. 2018). Line-of-sight velocities based on high-resolution optical spectroscopy are also available for these stars. The full space motion of each star can be reconstructed from these six parameters once a Galactic potential is adopted. We use these data to examine the kinematic properties of a large sample of highly *r*-process-enhanced field stars for the first time.

We present our sample of highly *r*-process-enhanced field stars in Section 2, and we present their astrometric and velocity data in Section 3. We describe our calculations of the kinematics in Section 4. We discuss the implications of these calculations in Section 5, and we summarize our conclusions in Section 6. Throughout this work, we adopt the standard nomenclature: for elements X and Y, [X/Y] is the abundance ratio relative to the solar ratio, defined as $\log_{10}(N_{\mathrm{X}}/N_{\mathrm{Y}}) - \log_{10}(N_{\mathrm{X}}/N_{\mathrm{Y}})_{\odot}$.

2. Sample Selection

Many highly *r*-process-enhanced stars have been identified and analyzed individually over the last 25 years. Our sample

Table 1
List of Known Highly *r*-process-enhanced Field Stars, Sorted by Decreasing [Eu/Fe] Ratios

Star	[Fe/H]	[Eu/Fe]	[Eu/H]	References
J235718.91−005247.8	−3.36	1.92	−1.44	Aoki et al. (2010)
HE 1523−0901	−2.95	1.81	−1.14	Frebel et al. (2007)
SMSS J1750460.30−425506.9	−2.17	1.75	−0.42	Jacobson et al. (2015)
CS 29497-004	−2.85	1.67	−1.18	Hill et al. (2017)
J203843.2−002333	−2.91	1.64	−1.27	Placco et al. (2017)
CS 22892-052	−3.10	1.64	−1.46	Sneden et al. (2003)
CS 31082-001	−2.90	1.63	−1.27	Hill et al. (2002)
J14325334−4125494	−2.79	1.61	−1.18	Hansen et al. (2018)
HE 1226−1149	−2.91	1.55	−1.36	Cohen et al. (2013)
J02462013−1518419	−2.71	1.45	−1.26	Hansen et al. (2018)
HE 1219−0312	−2.92	1.38	−1.54	Hayek et al. (2009)
HD 222925	−1.47	1.33	−0.14	Roederer et al. (2018)
J20093393−3410273	−1.99	1.32	−0.67	Hansen et al. (2018)
J21064294−6828266	−2.76	1.32	−1.44	Hansen et al. (2018)
J09544277+5246414	−2.99	1.28	−1.71	Holmbeck et al. (2018)
J15383085−1804242	−2.09	1.27	−0.82	Sakari et al. (2018)
SMSS J183128.71−341018.4	−1.83	1.25	−0.58	Howes et al. (2016)
J21091825−1310062	−2.40	1.25	−1.15	Hansen et al. (2018)
HE 0432−0923	−3.19	1.25	−1.94	Barklem et al. (2005)
CS 31078-018	−2.84	1.23	−1.61	Lai et al. (2008)
HE 0430−4901	−2.72	1.16	−1.56	Barklem et al. (2005)
CS 22183-031	−2.93	1.16	−1.77	Honda et al. (2004)
J23362202−5607498	−2.06	1.14	−0.92	Hansen et al. (2018)
SMSS J155430.57−263904.8	−2.61	1.14	−1.47	Jacobson et al. (2015)
CS 22945-058	−2.71	1.13	−1.58	Roederer et al. (2014a)
CS 22945-017	−2.73	1.13	−1.60	Roederer et al. (2014a)
J02165716−7547064	−2.50	1.12	−1.38	Hansen et al. (2018)
SMSS J183225.29−334938.4	−1.74	1.08	−0.66	Howes et al. (2016)
J19161821−5544454	−2.35	1.08	−1.27	Hansen et al. (2018)
HE 1127-1143	−2.73	1.08	−1.65	Barklem et al. (2005)
J17225742−7123000	−2.42	1.07	−1.35	Hansen et al. (2018)
SMSS J062609.83−590503.2	−2.77	1.06	−1.71	Jacobson et al. (2015)
J18024226−4404426	−1.55	1.05	−0.50	Hansen et al. (2018)
HE 2224+0143	−2.58	1.05	−1.53	Barklem et al. (2005)
CS 22953-003	−2.84	1.05	−1.79	François et al. (2007)
SMSS J175738.37−454823.5	−2.46	1.02	−1.44	Jacobson et al. (2015)
CS 22958-052	−2.42	1.00	−1.42	Roederer et al. (2014a)
SMSS J024858.41−684306.4	−3.71	1.00	−2.71	Jacobson et al. (2015)
J18174532−3353235	−1.67	0.99	−0.68	Johnson et al. (2013)
HE 2301−4024	−2.11	0.98	−1.13	Barklem et al. (2005)
HE 2327−5642	−2.78	0.98	−1.80	Mashonkina et al. (2010)
CS 29491-069	−2.55	0.96	−1.59	Hayek et al. (2009)
SMSS J181505.16−385514.9	−3.29	0.96	−2.33	Howes et al. (2015)
HE 2244−1503	−2.88	0.95	−1.93	Barklem et al. (2005)
SMSS J051008.62−372019.8	−3.20	0.95	−2.25	Jacobson et al. (2015)
SMSS J221448.33−453949.9	−2.56	0.94	−1.62	Jacobson et al. (2015)
HE 1044−2509	−2.89	0.94	−1.95	Barklem et al. (2005)
J19014952−4844359	−1.87	0.93	−0.94	Hansen et al. (2018)
CS 22875-029	−2.69	0.92	−1.77	Roederer et al. (2014a)
BD +17°3248	−2.06	0.91	−1.15	Cowan et al. (2002)
J19324858−5908019	−1.93	0.90	−1.03	Hansen et al. (2018)
CS 29529-054	−2.75	0.90	−1.85	Roederer et al. (2014a)
J21224590−4641030	−2.96	0.90	−2.06	Hansen et al. (2018)
J15582962−1224344	−2.54	0.89	−1.65	Hansen et al. (2018)
SMSS J063447.15−622355.0	−3.41	0.89	−2.52	Jacobson et al. (2015)
HE 1131+0141	−2.48	0.87	−1.61	Barklem et al. (2005)
J00405260−5122491	−2.11	0.86	−1.25	Hansen et al. (2018)
CS 22888-047	−2.54	0.86	−1.68	Roederer et al. (2014a)
CS 22943-132	−2.67	0.86	−1.81	Roederer et al. (2014a)
CS 22896-154	−2.69	0.86	−1.83	François et al. (2007)
CS 30306-132	−2.42	0.85	−1.57	Honda et al. (2004)
CS 22886-012	−2.61	0.85	−1.76	Roederer et al. (2014a)
HD 115444	−2.96	0.85	−2.11	Westin et al. (2000)
SMSS J183647.89−274333.1	−2.48	0.82	−1.66	Howes et al. (2015)

Table 1
(Continued)

Star	[Fe/H]	[Eu/Fe]	[Eu/H]	References
CS 22882-001	−2.62	0.81	−1.81	Roederer et al. (2014a)
HE 2252−4225	−2.63	0.81	−1.82	Mashonkina et al. (2014)
HD 20	−1.58	0.80	−0.78	Barklem et al. (2005)
HD 221170	−2.18	0.80	−1.38	Ivans et al. (2006)
HE 0420+0123a	−3.03	0.79	−2.24	Hollek et al. (2011)
HE 0300−0751	−2.27	0.77	−1.50	Barklem et al. (2005)
J21095804−0945400	−2.73	0.77	−1.96	Hansen et al. (2018)
J19232518−5833410	−2.08	0.76	−1.32	Hansen et al. (2018)
J19215077−4452545	−2.56	0.74	−1.80	Hansen et al. (2018)
SMSS J195931.70−643529.3	−2.58	0.74	−1.84	Jacobson et al. (2015)
J17435113−5359333	−2.24	0.73	−1.51	Hansen et al. (2018)
HE 0240−0807	−2.68	0.73	−1.95	Barklem et al. (2005)
BS 17569-049	−2.88	0.72	−2.16	François et al. (2007)
HE 1430+0053	−3.03	0.72	−2.31	Barklem et al. (2005)
CS 30315-029	−3.33	0.72	−2.61	Barklem et al. (2005)
J01530024−3417360	−1.50	0.71	−0.79	Hansen et al. (2018)
J15271353−2336177	−2.15	0.70	−1.45	Hansen et al. (2018)
J18294122−4504000	−2.48	0.70	−1.78	Hansen et al. (2018)
SMSS J182601.24−332358.3	−2.83	0.70	−2.13	Howes et al. (2016)

includes stars from the literature that show at least moderately high levels of *r*-process enhancement relative to Fe, $[\mathrm{Eu/Fe}] \geqslant +0.7$; i.e., enhanced by a factor of 5 relative to the solar ratio. Europium (Eu, $Z = 63$) is commonly used as a proxy for the overall level of *r*-process enhancement in a star. A large fraction (≈94%–98%; Sneden et al. 2008; Bisterzo et al. 2011) of the Eu in the solar system originated via the *r*-process, despite the fact that both the *r*-process and the *s*-process (slow neutron-capture process) contributed roughly equal amounts to the total mass of elements heavier than the Fe group in the solar system. We also require that the heavy-element abundance pattern in each star has been scrutinized in sufficient detail to determine that the *r*-process was the dominant source of the heavy elements (e.g., Sneden et al. 1996). We only include field stars in our sample, so *r*-process-enhanced stars in dwarf galaxies and globular clusters are not considered.

Table 1 lists the 83 stars satisfying our criteria, along with the metallicity ([Fe/H]), europium-to-iron ratio ([Eu/Fe]), europium-to-hydrogen ratio ([Eu/H]), and the literature references for these abundances. We only calculate kinematic and orbital properties for the subset of stars in Table 1 with relatively small uncertainties in their parallax measurements, as discussed in Section 3. We retain all 83 stars in Table 1 as a reference, however, anticipating that better distance estimates will be available in the future.

We emphasize that the sample in Table 1 is subject to strong observational biases. Most of these stars were recognized as being *r*-process-enhanced during high-resolution spectroscopic follow-up of metal-poor candidates identified via objective-prism surveys (Bidelman & MacConnell 1973; Bond 1980; Beers et al. 1985, 1992; Christlieb et al. 2008). Many observers contributed to these efforts over the decades, and their decisions regarding which stars to observe are somewhat subjective and not easily quantified.

Our definition of a highly *r*-process-enhanced star differs slightly from that found in the literature. The common "*r*-II" designation (Beers & Christlieb 2005) refers to stars with $[\mathrm{Eu/Fe}] > +1.0$ and $[\mathrm{Ba/Eu}] < 0$, while the "*r*-I" designation refers to stars with more moderate enhancement, $+0.3 \leqslant [\mathrm{Eu/Fe}] \leqslant +1.0$ and $[\mathrm{Ba/Eu}] < 0$. The boundaries defining these classifications are arbitrary. Our choice of $[\mathrm{Eu/Fe}] \geqslant +0.7$ is motivated by the upper envelope of $[\mathrm{Eu/Fe}] \approx +0.6$ found in most globular clusters (e.g., Gratton et al. 2004), kinematically selected samples of disk stars (e.g., Venn et al. 2004; Battistini & Bensby 2016), and stars toward the Galactic bulge (e.g., Johnson et al. 2012). $[\mathrm{Eu/Fe}] \geqslant +0.7$ may represent a more natural and physically interpretable lower limit for the class of highly *r*-process-enhanced stars than the $[\mathrm{Eu/Fe}] > +1.0$ criterion commonly adopted for *r*-II stars, as we discuss in Section 5.4.

Figure 1 displays the [Eu/H] and [Eu/Fe] ratios for stars in our sample. [Eu/H] provides an estimate of the amount of dilution of *r*-process material into gas, and [Eu/Fe] provides an estimate of the amount of *r*-process material relative to the amount of Fe and other metals from supernovae. The *r*-process-enhanced stars in Reticulum II (Ret II; Ji et al. 2016b; Roederer et al. 2016), the one known highly *r*-process-enhanced galaxy, are shown for comparison. These stars span a range of ≈1 dex in [Eu/H], [Eu/Fe], and [Fe/H], indicating that stars within an individual dwarf galaxy exhibit different levels of *r*-process enrichment from a single *r*-process event. Figure 2 illustrates a T_{eff}–$\log g$ diagram for the stars in our sample. These stars span a range of evolutionary states, from main-sequence stars to the red horizontal branch.

3. Input Kinematic Data

Table 2 lists the *Gaia* DR2 source ID, parallax (ϖ), proper motions ($\mu_{\alpha} \cos\delta$, μ_{δ}), distance, heliocentric radial velocity (RV), and 1σ uncertainties for each of these quantities. The ϖ, $\mu_{\alpha} \cos\delta$, and μ_{δ} values are adopted from *Gaia* DR2 (Lindegren et al. 2018). The distances reported in Table 2 are adopted from Bailer-Jones et al. (2018) and are based on *Gaia* DR2 parallaxes. Literature references are given for the RV measurements from high-resolution optical spectroscopy. We estimate the RV uncertainty based on the data quality when previous studies did not explicitly state this value. The systemic RV is listed for known RV-variable stars, when available (e.g.,

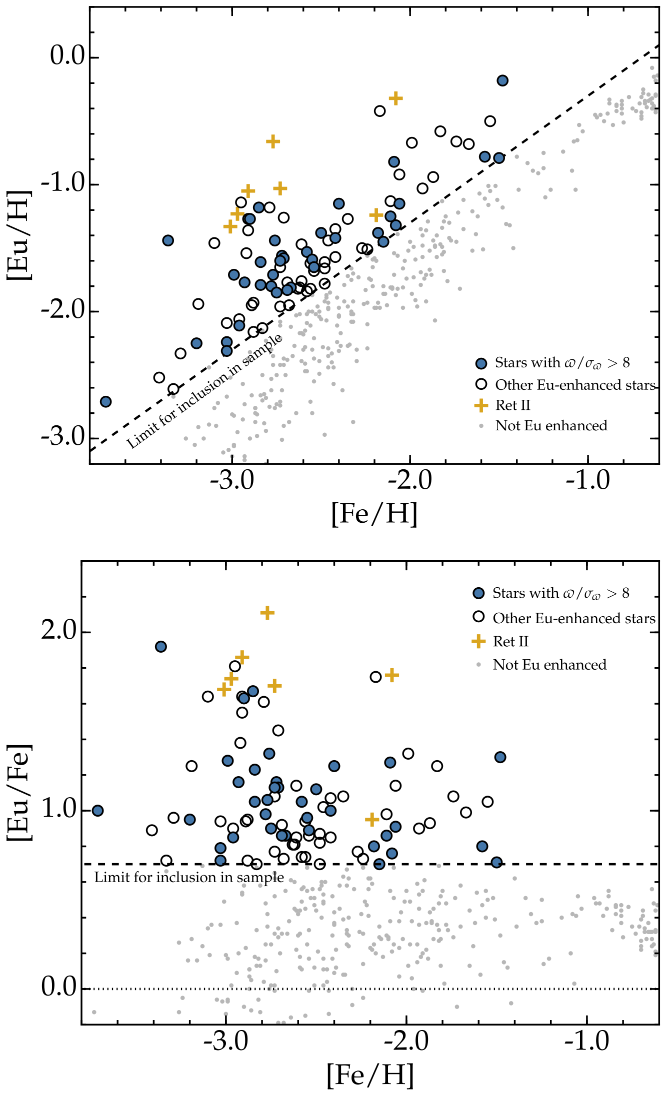

Figure 1. The [Eu/H] (top) and [Eu/Fe] (bottom) ratios as a function of [Fe/H] for stars included in our sample. Stars meeting our parallax requirement, $\varpi/\sigma_\varpi \geqslant 8.0$, are indicated by filled circles. All other highly *r*-process-enhanced stars are indicated by open circles. The yellow crosses mark stars in the Ret II UFD galaxy. The small gray points mark other stars from Barklem et al. (2005), Roederer et al. (2014b), Jacobson et al. (2015), Battistini & Bensby (2016), and Hansen et al. (2018). The dashed line marks the lower limit of [Eu/Fe] $\geqslant +0.7$ for inclusion in our sample. The dotted line in the bottom panel marks the solar [Eu/Fe] ratio.

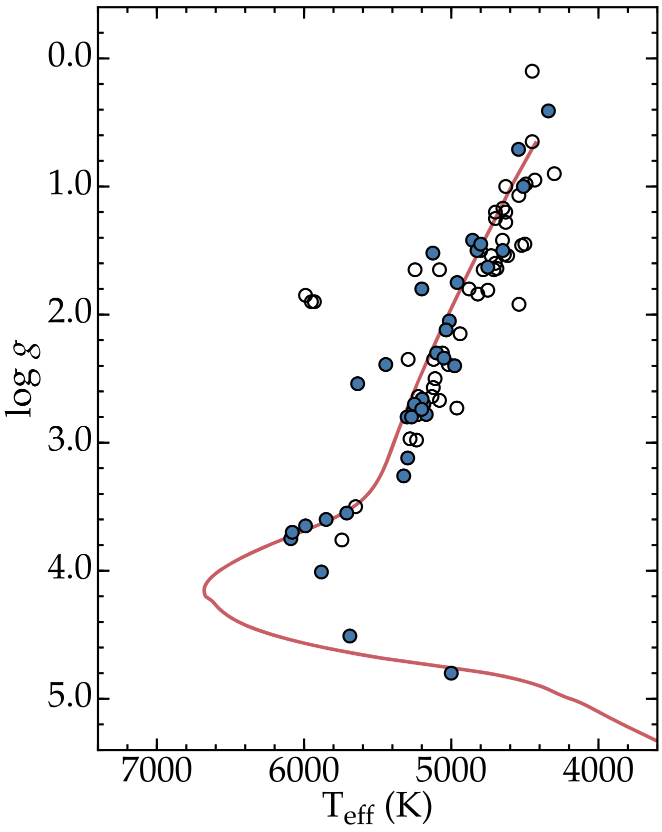

Figure 2. Location of the 83 stars in our sample on a $T_{\rm eff}$–log g diagram. Stars meeting our parallax requirement, $\varpi/\sigma_\varpi \geqslant 8.0$, are indicated by filled circles. All other highly *r*-process-enhanced stars are indicated by open circles. The red line is a 13 Gyr isochrone for a metal-poor ([Fe/H] $= -2.5$), α-enhanced ([α/Fe] $= +0.4$) stellar population with a standard He mass fraction (0.2452) downloaded from the Dartmouth Stellar Evolution Database (Dotter et al. 2008).

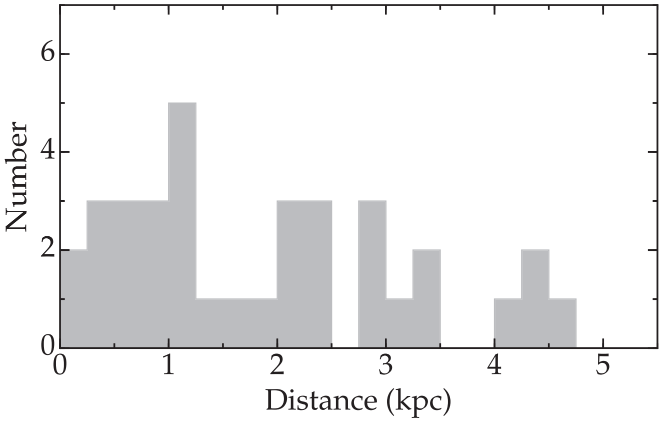

Figure 3. Histogram of estimated distances (Bailer-Jones et al. 2018) to the 35 highly *r*-process-enhanced stars in our sample.

Hansen et al. 2015). The *Gaia* RV measurements agree with literature values to within ≈2–3 km s^{-1}.

We impose a parallax cut on our sample, requiring that $\varpi/\sigma_\varpi \geqslant 8.0$ (i.e., 12.5% errors or better). We determine this value empirically, and larger parallax uncertainties generally yield orbital properties and integrals of motion (Section 4) that are highly uncertain. Thirty-five stars pass this cut for further examination. These stars represent a local sample, as shown in Figure 3. The median distance is 1.6 kpc, and 80% of the sample is located within 3 kpc of the Sun.

4. Energy, Actions, and Orbital Calculations

We convert the observed astrometric quantities into orbital parameters and integrals of motion for each star in our sample. We assume that the Sun is on the Galactic plane (Bovy 2017) and is $R_0 = 8.0$ kpc away from the Galactic center. We also assume that the circular velocity at the solar position is $v_0 = 220$ km s^{-1} and the solar peculiar velocity relative to the circular velocity is $(U_\odot, V_\odot, W_\odot) = (11.1, 12.24, 7.25)$ km s^{-1} (Schönrich et al. 2010). We adopt the realistic gravitational potential model `MWPotential2014` (Bovy 2015), which assumes a virial mass of $0.8 \times 10^{12} M_\odot$. Our calculations account for the correlations between $\mu_\alpha \cos\delta$ and μ_δ, ϖ and $\mu_\alpha \cos\delta$, and ϖ and μ_δ as reported by *Gaia* DR2.

Table 2
Parallaxes, Proper Motions, Distances, and Radial Velocities

Star	*Gaia* DR2 source ID	ϖ (mas)	Unc. (mas)	$\mu_\alpha \cos \delta$ (mas yr^{-1})	Unc. (mas yr^{-1})	μ_δ (mas yr^{-1})	Unc. (mas yr^{-1})	Distance (kpc)	− (kpc)	+ (kpc)	RV (km s^{-1})	Unc. (km s^{-1})	RV References
J235718.91−005247.8	2449797054412948224	1.8683	0.0550	49.753	0.089	−172.407	0.051	0.527	0.015	0.016	−9.4	0.5	Aoki et al. (2010)
CS 29497-004	2322729725405593728	0.2396	0.0299	9.473	0.049	0.392	0.042	3.474	0.319	0.384	105.0	0.4	Hansen et al. (2015)
CS 31082-001	2451773941958712192	0.4806	0.0462	11.745	0.093	−42.709	0.038	1.913	0.155	0.183	139.1	0.1	Hansen et al. (2015)
HD 222925	6487799171512458624	2.2332	0.0243	154.854	0.041	−99.171	0.041	0.442	0.005	0.005	−38.9	0.6	Roederer et al. (2018)
J21064294−6828266	6376678403241698560	0.4489	0.0297	−4.429	0.034	−18.376	0.045	2.089	0.124	0.141	−72.6	0.6	Hansen et al. (2018)
J09544277+5246414	828438619475671936	0.3061	0.0357	−17.897	0.050	−26.914	0.049	2.809	0.251	0.301	−67.7	1.0	Holmbeck et al. (2018)
J15383085−1804242	6255142030043852928	0.9629	0.0399	−49.471	0.091	−37.986	0.060	1.010	0.040	0.043	131.3	0.5	Sakari et al. (2018)
J21091825−1310062	6885782695269539584	0.4254	0.0429	3.183	0.069	−28.673	0.052	2.190	0.193	0.233	−35.9	0.4	Hansen et al. (2018)
CS 31078-018	7189878332862720	0.6440	0.0300	17.350	0.057	−10.216	0.048	1.479	0.063	0.069	81.3	0.2	Lai et al. (2008)
HE 0430−4901	4787830774791048832	0.3698	0.0170	7.281	0.029	4.822	0.037	2.491	0.101	0.110	208.7	3.0	Barklem et al. (2005)
CS 22945-058	6389179335052544256	0.5849	0.0250	30.739	0.037	−22.226	0.036	1.627	0.064	0.069	23.4	0.5	Roederer et al. (2014b)
CS 22945-017	6486692891016362240	0.7907	0.0212	29.925	0.031	−3.596	0.031	1.220	0.031	0.033	101.8	0.8	Roederer et al. (2014b)
J02165716−7547064	4637170571951777280	0.1824	0.0215	−3.367	0.038	1.648	0.032	4.474	0.381	0.453	−5.8	0.3	Hansen et al. (2018)
SMSS J062609.83 −590503.2	5482786685494509056	0.1907	0.0169	2.073	0.034	2.140	0.035	4.402	0.302	0.347	−110.0	1.0	Jacobson et al. (2015)
HE 2224+0143	2703430605705583360	0.3207	0.0369	4.073	0.043	−10.241	0.043	2.762	0.256	0.310	−113.1	0.2	Hansen et al. (2015)
CS 22953-003	4710594687144052096	0.2101	0.0141	−3.819	0.029	−15.767	0.022	4.101	0.224	0.250	208.5	0.3	Bonifacio et al. (2009), Roederer et al. (2014b)
CS 22958-052	4742398404575483648	0.8491	0.0163	37.371	0.028	9.317	0.028	1.139	0.021	0.022	88.9	0.8	Roederer et al. (2014b)
SMSS J024858.41 −684306.4	4647065936083474816	0.2687	0.0157	−5.104	0.030	−8.605	0.027	3.318	0.166	0.183	−239.2	1.0	Jacobson et al. (2015)
HE 2327−5642	6495850379767072128	0.1779	0.0201	12.569	0.026	−8.692	0.026	4.595	0.379	0.448	282.2	1.0	Mashonkina et al. (2010) [a]
CS 29491-069	6600971319243174144	0.3857	0.0326	10.055	0.046	−34.609	0.049	2.386	0.174	0.202	−377.1	0.7	Hayek et al. (2009)
SMSS J051008.62 −372019.8	4820909925710430976	0.9051	0.0291	11.816	0.038	−23.439	0.046	1.070	0.033	0.035	372.8	1.0	Jacobson et al. (2015)
BD +17°3248	4553184509407224576	1.2209	0.0359	−47.746	0.064	−22.412	0.067	0.801	0.023	0.024	−145.2	0.8	Behr (2003)
CS 29529-054	4679456071169507712	0.9797	0.0199	28.701	0.032	−28.615	0.037	0.991	0.019	0.020	113.2	0.4	Roederer et al. (2014b)
J15582962−1224344	4342895871148449152	0.4103	0.0335	−8.824	0.069	−0.691	0.041	2.284	0.166	0.193	83.1	0.5	Hansen et al. (2018)
J00405260−5122491	4925248047268557056	6.6710	0.0274	211.493	0.036	−197.324	0.037	0.149	0.001	0.001	123.1	0.2	Hansen et al. (2018)
CS 22943-132	6679228303437917696	2.1670	0.0242	68.310	0.039	−43.701	0.026	0.456	0.005	0.005	18.9	0.8	Roederer et al. (2014b)
CS 22896-154	6448440159932433536	0.3074	0.0181	−9.747	0.028	−24.965	0.024	2.971	0.156	0.172	137.9	1.0	Bonifacio et al. (2009)
HD 115444	1474455748663044736	1.1989	0.0403	4.556	0.051	−60.449	0.054	0.815	0.026	0.028	−27.0	0.5	Hansen et al. (2015)
HD 20	2333756864959936000	1.9447	0.0527	132.434	0.066	−39.917	0.058	0.507	0.013	0.014	−57.9	0.1	Hansen et al. (2015)
HD 221170	2869759781250083200	1.8370	0.0587	−16.642	0.080	−53.664	0.059	0.536	0.017	0.018	−121.2	0.1	Hansen et al. (2015)
HE 0420+0123a	3279770347306973056	0.8934	0.0427	33.257	0.076	−21.424	0.044	1.083	0.048	0.053	−55.3	1.0	Hollek et al. (2011)
J19232518−5833410	6638565923901510656	0.4567	0.0548	−23.412	0.072	−16.432	0.048	2.072	0.218	0.275	125.9	0.6	Hansen et al. (2018)
HE 1430+0053	3653467682134558592	0.2980	0.0304	−23.168	0.053	−14.932	0.044	3.009	0.253	0.302	−107.7	0.4	Hansen et al. (2015)
J01530024−3417360	5017240268153817600	3.2385	0.0386	22.189	0.041	−212.060	0.045	0.306	0.004	0.004	22.8	0.4	Hansen et al. (2018)
J15271353−2336177	6239162964995926016	6.7911	0.0456	−228.893	0.095	−96.951	0.066	0.147	0.001	0.001	1.2	0.3	Hansen et al. (2018)

Notes. The − and + columns indicate the 16th percentile and 84th percentile confidence intervals.

[a] The median RV from this source is adopted as the systemic RV.

Table 3
Calculated Velocities in a Cylindrical Coordinate System

Star	V_R	−	+	V_ϕ	−	+	V_z	−	+	$V_\perp$	−	+
	(km s^{-1})			(km s^{-1})			(km s^{-1})			(km s^{-1})		
J235718.91−005247.8	−118.3	5.7	5.6	−154.4	18.4	17.6	−204.7	10.6	10.2	236.4	11.5	12.1
CS 29497-004	153.2	23.7	37.2	145.7	21.8	13.4	−114.2	3.9	2.5	191.0	20.1	33.1
CS 31082-001	−130.6	14.0	12.2	−161.6	34.5	30.2	−193.3	5.7	5.1	233.3	10.9	12.7
HD 222925	246.9	4.3	4.8	−52.2	5.6	5.0	68.5	0.7	0.7	256.2	4.3	4.8
J21064294−6828266	56.9	3.5	4.8	100.8	15.8	12.8	142.9	7.4	9.0	153.8	8.0	10.2
J09544277+5246414	161.9	23.3	25.8	−237.0	65.0	55.3	−119.4	11.0	9.4	201.2	23.8	27.6
J15383085−1804242	−52.3	3.2	3.5	−88.0	13.2	11.8	96.3	1.0	1.1	109.6	0.7	0.8
J21091825−1310062	−84.4	14.6	11.7	−52.2	24.0	20.8	−102.8	13.2	11.1	133.2	16.0	19.3
CS 31078-018	91.2	2.4	2.7	99.3	9.1	7.9	−28.8	1.2	1.4	95.6	1.9	2.2
HE 0430−4901	98.4	7.6	9.7	68.8	2.0	2.1	−71.4	6.3	7.9	121.9	3.1	4.2
CS 22945-058	158.5	12.2	15.0	−6.1	14.5	12.0	41.4	3.0	3.7	163.9	12.7	15.4
CS 22945-017	85.9	7.3	8.3	114.8	3.4	3.1	−121.9	2.8	2.5	149.0	5.9	7.3
J02165716−7547064	−194.0	56.5	34.2	240.9	25.4	9.2	−46.5	16.7	10.3	199.5	35.7	59.0
SMSS J062609.83−590503.2	−126.1	15.5	12.4	280.4	13.3	9.2	109.0	9.2	15.2	166.9	15.4	21.8
HE 2224+0143	5.0	6.7	4.7	36.1	16.0	11.9	−17.0	15.1	11.0	18.1	6.2	14.0
CS 22953-003	−274.9	17.9	18.2	−154.7	87.0	51.7	31.1	28.8	45.4	277.1	19.9	26.7
CS 22958-052	155.0	8.3	8.6	92.3	3.7	3.7	−26.1	1.8	2.1	157.2	7.8	8.2
SMSS J024858.41−684306.4	−255.4	45.5	34.9	336.1	24.6	16.2	222.0	5.8	7.4	338.3	29.6	40.4
HE 2327−5642	156.9	67.4	125.0	−138.9	31.3	36.7	−230.3	1.3	1.2	279.1	32.2	85.4
CS 29491-069	157.0	4.7	3.6	−262.2	47.9	40.3	271.5	6.5	5.8	313.6	7.9	6.8
SMSS J051008.62−372019.8	43.6	4.1	3.5	−114.4	4.2	3.6	−175.1	1.4	1.6	180.5	2.4	2.2
BD +17°3248	37.5	2.1	1.9	−8.6	4.9	4.7	68.1	3.9	3.9	77.8	2.4	2.6
CS 29529-054	−93.1	2.9	2.5	20.0	6.2	5.2	64.4	5.1	6.1	113.1	4.8	6.0
J15582962−1224344	−47.2	3.2	4.1	156.6	8.2	6.3	110.4	5.6	6.8	120.0	3.8	5.0
J00405260−5122491	20.9	0.4	0.4	2.8	1.1	1.2	−53.6	0.4	0.4	57.5	0.2	0.2
CS 22943-132	66.4	1.7	1.9	158.3	1.4	1.2	−135.0	2.5	2.4	150.4	2.8	3.0
CS 22896-154	−6.3	21.1	32.9	−209.3	52.7	42.8	38.6	10.7	13.9	41.6	3.6	17.3
HD 115444	−166.1	5.2	5.2	52.0	5.8	5.4	16.6	1.2	1.3	166.9	5.3	5.3
HD 20	234.0	4.7	4.9	−7.4	4.9	4.6	6.2	1.2	1.1	234.1	4.7	4.9
HD 221170	−128.3	1.9	2.1	102.0	0.5	0.4	−33.2	2.0	2.1	132.5	2.5	2.4
HE 0420+0123a	−56.3	0.9	0.8	44.5	9.5	8.2	107.8	2.9	3.5	121.6	2.7	3.3
J19232518−5833410	−125.6	1.6	2.4	−50.1	22.5	20.5	141.6	16.0	17.6	189.2	10.5	12.1
HE 1430+0053	183.7	18.5	25.0	−164.3	60.1	48.1	−45.1	4.0	5.3	189.2	16.7	23.3
J01530024−3417360	−189.0	2.1	2.2	−26.0	3.1	3.2	26.0	0.6	0.6	190.8	2.3	2.2
J15271353−2336177	56.4	0.5	0.4	78.8	1.0	0.8	50.1	0.3	0.3	75.4	0.4	0.5

Note. The − and + columns indicate the 16th percentile and 84th percentile confidence intervals.

We sample 10^3 sets of (ϖ, ℓ, b, RV, $\mu_\alpha \cos\delta$, μ_δ) from the error distribution of each quantity for each star, where the uncertainties in ℓ and b (Galactic longitude and latitude, respectively) are negligible. This exercise yields 10^3 samples of the six-dimensional positions and velocities for each star. We use the publicly available `Agama` code (Vasiliev 2018) to calculate the corresponding stellar orbits over 3 Gyr for each sample, yielding pericentric radius ($r_{\rm peri}$), apocentric radius ($r_{\rm apo}$), maximum height above or below the Galactic midplane ($Z_{\rm max}$), and eccentricity ($e = (r_{\rm apo} - r_{\rm peri})/(r_{\rm apo} + r_{\rm peri})$). We also use `Agama`, which implements an efficient algorithm by Binney (2012), to evaluate the integrals of motion. This yields the specific orbital energy ($E = (1/2)\boldsymbol{v}^2 + \Phi(\boldsymbol{x})$; hereafter "energy") and three-dimensional action ($\boldsymbol{J} = (J_r, J_\phi, J_z)$). We define the radial and vertical actions, J_r and J_z, in the same manner as Binney (2012). J_r is defined to be non-negative, and its value can be interpreted as the extent of the radial excursion of an orbit. For a given E, $J_r = 0$ for circular orbits or shell-like orbits, and J_r is large for eccentric orbits. J_z is also non-negative, and its value can be interpreted as the extent of the vertical excursion of an orbit. For example, $J_z = 0$ for planar orbits, and J_z is large for orbits with large $Z_{\rm max}$. We define the azimuthal action by

$$J_\phi = \frac{1}{2\pi} \oint_{\rm orbit} d\phi \, RV_\phi = -L_z, \tag{1}$$

such that prograde stars have $J_\phi > 0$ and $V_\phi > 0$. Note that $\pi \simeq 3.14$ is a mathematical constant, and ϖ denotes the parallax.

Table 3 lists, for each star meeting our $\varpi/\sigma_\varpi \geqslant 8.0$ requirement, the calculated median velocities in a cylindrical coordinate system (V_R, V_ϕ, V_z) and $V_\perp$, defined as $(V_R^2 + V_z^2)^{1/2}$. Table 4 lists the calculated median actions (J_r, J_ϕ, J_z) and energy (E). Table 5 lists the calculated median values for $r_{\rm peri}$, $r_{\rm apo}$, $Z_{\rm max}$, and e. The columns indicated by a minus or plus sign represent the difference between the median and the 16th and 84th percentiles (analogous to the 1σ range) of each quantity.

5. Discussion

5.1. Kinematic and Orbital Properties of Highly r-process-enhanced Stars in the Solar Neighborhood

In this section, we discuss general kinematic and orbital properties of the ensemble of highly *r*-process-enhanced stars and highlight characteristics of a few individual stars. Figure 4

Table 4

Calculated Orbital Energies and Angular Momenta

Star	E	−	+	J_r	−	+	J_ϕ	−	+	J_z	−	+
	(10^3 km^2 s^{-2})			(kpc km s^{-1})			(kpc km s^{-1})			(kpc km s^{-1})		
J235718.91−005247.8	−91.8	5.2	5.9	264	80.4	142	−1210	148	141	760	27.7	28.2
CS 29497-004	−94.0	3.1	6.4	608	176	352	1150	176	110	254	14.2	41.7
CS 31082-001	−86.1	7.3	9.6	291	146	333	−1340	302	261	947	4.8	13.3
HD 222925	−98.2	1.3	1.5	1080	18.0	23.6	−378	43.8	38.9	90.4	2.6	2.8
J21064294−6828266	−120	0.3	0.6	58.3	3.9	2.1	692	116	96.5	420	64.5	93.1
J09544277+5246414	−70.1	17.4	25.0	882	592	2600	−2360	745	605	527	61.5	86.8
J15383085−1804242	−127	0.7	0.9	222	41.5	38.4	−599	90.0	81.0	146	1.3	1.4
J21091825−1310062	−128	2.4	3.8	265	87.9	93.8	−320	149	133	293	68.4	80.6
CS 31078-018	−114	0.2	0.3	375	37.0	45.0	938	76.1	65.2	26.4	0.6	0.8
HE 0430−4901	−115	1.0	1.4	473	32.1	40.6	634	20.0	20.0	106	14.1	15.4
CS 22945-058	−120	1.9	2.7	704	25.8	21.7	−16.5	105	87.7	106	18.8	26.5
CS 22945-017	−115	0.4	0.6	197	21.2	25.5	880	28.8	26.8	220	8.4	9.4
J02165716−7547064	−77.8	6.3	11.8	827	265	677	1760	142	59.8	445	164	407
SMSS J062609.83−590503.2	−66.6	2.3	4.2	1230	148	297	2670	32.4	77.0	183	34.5	62.8
HE 2224+0143	−130	0.1	0.5	439	37.5	44.0	293	120	90.8	77.0	14.6	30.4
CS 22953-003	−77.5	13.3	27.0	1350	410	2210	−1060	588	354	404	45.3	155
CS 22958-052	−114	0.9	1.0	510	38.1	41.3	759	29.3	29.3	22.6	0.7	1.0
SMSS J024858.41−684306.4	−13.4	5.2	7.7	24200	7770	31300	2580	181	123	343	7.4	4.4
HE 2327−5642	−80.6	14.8	37.0	1260	713	3930	−788	117	182	592	110	273
CS 29491-069	−51.5	7.6	11.1	2970	916	2030	−1740	281	246	1080	89.4	105
SMSS J051008.62−372019.8	−106	0.2	0.3	59.9	7.7	6.4	−936	38.5	32.3	650	17.4	15.6
BD +17°3248	−132	0.1	0.1	566	31.9	20.5	−36.3	36.2	35.0	57.8	8.1	9.1
CS 29529-054	−124	0.4	0.6	596	18.8	22.0	190	49.4	41.4	58.5	9.9	13.8
J15582962−1224344	−123	1.9	1.5	21.3	1.7	2.0	943	84.0	67.4	193	22.4	28.9
J00405260−5122491	−130	0.1	0.1	608	7.3	6.2	52.2	8.8	9.8	33.0	0.6	0.6
CS 22943-132	−109	0.2	0.2	73.0	3.3	3.9	1240	11.5	10.7	251	10.7	11.4
CS 22896-154	−124	6.6	11.8	25.8	22.3	79.5	−1110	192	185	90.1	26.2	49.6
HD 115444	−115	0.6	0.6	665	34.2	36.9	446	46.2	43.0	27.7	2.6	3.1
HD 20	−104	1.1	1.2	1210	26.7	16.5	−28.9	38.6	36.2	10.8	0.1	0.1
HD 221170	−116	0.3	0.3	393	5.2	5.4	858	3.5	3.2	15.8	1.9	2.1
HE 0420+0123a	−117	0.2	0.2	387	21.8	23.4	432	83.3	71.2	285	30.9	42.2
J19232518−5833410	−123	1.9	2.8	397	75.5	82.9	−288	129	124	259	58.9	64.8
HE 1430+0053	−105	9.5	16.3	322	38.6	275	−975	300	266	314	52.2	96.4
J01530024−3417360	−113	0.5	0.5	895	3.1	4.2	−178	24.6	25.5	6.1	0.2	0.2
J15271353−2336177	−126	0.1	0.1	334	2.8	3.5	650	7.6	6.3	24.6	0.3	0.4

Note. The − and + columns indicate the 16th percentile and 84th percentile confidence intervals.

shows the relationships between [Fe/H] and our calculated orbital and kinematic properties. Different symbol shapes and colors are used in Figure 4 to indicate the different groups of stars identified by our clustering analysis (Section 5.2). For now, we disregard these classifications.

None of the stars in our sample have disk-like kinematics, as shown in Figure 5. For comparison, Figure 5 also shows a sample of 10,385 disk stars located within 200 pc of the Sun with $-0.25 < \mathrm{[Fe/H]} < +0.25$ (cf. Hattori et al. 2018a), selected from the Tycho-*Gaia* Astrometric Solution (TGAS; Lindegren et al. 2016) and RAdial Velocity Experiment (RAVE DR5; Kunder et al. 2017). There is virtually no velocity overlap between these disk stars and the highly *r*-process-enhanced stars. If the stars in our sample are not on disk-like orbits, then presumably they must have been formed in situ in the halo, formed in the disk or bulge and ejected into halo orbits, or accreted. We argue in Section 5.4 that the accretion origin is likely for most of these stars.

All of the highly *r*-process-enhanced stars in our sample are bound to the Milky Way ($E < 0$; see Figure 4). There are roughly equal numbers of stars moving toward ($V_{\mathrm{R}} < 0$) and away from the Galactic center ($V_{\mathrm{R}} > 0$), and there are roughly equal numbers of stars moving north ($V_z > 0$) and south ($V_z < 0$) as they pass through the Galactic disk. There are also roughly equal numbers of stars on prograde (V_ϕ or $J_\phi > 0$) and retrograde (V_ϕ or $J_\phi < 0$) orbits, and the net rotation for this sample of 35 stars is consistent with zero (unweighted mean $V_\phi = 7 \pm 24$ km s^{-1}, with standard deviation 142 km s^{-1}). The relative balance in these quantities would indicate that phase-mixing has occurred among an accreted population.

Most of the stars in our sample always remain in the inner regions of the Galactic halo. Figure 6 shows histograms of their r_{peri}, r_{apo}, and $Z_{\max}$ values. Many of the stars (77%) are on eccentric ($e > 0.5$), radial orbits, and 66% of the stars have $r_{\mathrm{apo}} < 13$ kpc, indicating that they are at or near apocenter while in the solar neighborhood. More than 51% of the stars pass within 2.6 kpc of the Galactic center at pericenter, and 20% of the sample passes within 1 kpc. Most of the stars (71%) travel at least 3 kpc above or below the Galactic plane, and 20% of the stars orbit beyond r_{apo} or $Z_{\max} > 20$ kpc.

The star in our sample with the highest energy, SMSS J024858.41−684306.4 ([Fe/H] = −3.71, [Eu/H] = −2.71,

Table 5
Calculated Orbital Parameters

Star	r_{peri}	−	+	r_{apo}	−	+	Z_{max}	−	+	e	−	+
	(kpc)			(kpc)			(kpc)					
J235718.91−005247.8	6.60	0.43	0.32	15.9	2.41	3.40	12.0	1.88	2.48	0.414	0.041	0.059
CS 29497-004	3.71	0.71	0.56	16.9	1.81	3.89	8.24	1.27	2.94	0.641	0.081	0.109
CS 31082-001	7.86	0.38	0.21	18.5	4.11	7.29	14.6	2.68	4.80	0.403	0.088	0.120
HD 222925	0.99	0.07	0.07	16.6	0.52	0.64	5.28	0.08	0.09	0.888	0.003	0.004
J21064294−6828266	3.96	0.10	0.18	7.19	0.06	0.06	5.20	0.43	0.52	0.289	0.016	0.010
J09544277+5246414	8.67	1.30	0.79	30.6	13.2	43.2	16.9	6.96	20.1	0.559	0.152	0.213
J15383085−1804242	2.02	0.32	0.39	7.42	0.05	0.05	3.21	0.10	0.10	0.571	0.065	0.058
J21091825−1310062	1.57	0.83	0.85	7.28	0.12	0.22	5.23	0.08	0.28	0.644	0.133	0.168
CS 31078-018	2.56	0.27	0.24	10.4	0.09	0.11	1.41	0.04	0.05	0.605	0.032	0.037
HE 0430−4901	1.81	0.08	0.11	10.5	0.37	0.44	3.53	0.18	0.23	0.706	0.012	0.012
CS 22945-058	0.17	0.10	0.20	9.72	0.22	0.52	4.55	0.41	0.33	0.965	0.037	0.020
CS 22945-017	3.30	0.14	0.14	9.20	0.20	0.26	4.58	0.21	0.26	0.472	0.025	0.027
J02165716−7547064	6.27	0.05	0.25	25.9	4.80	12.1	14.6	5.01	13.2	0.611	0.068	0.095
SMSS J062609.83−590503.2	8.04	0.07	0.21	36.4	2.78	5.58	11.6	1.85	3.64	0.638	0.021	0.034
HE 2224+0143	1.10	0.35	0.03	7.76	0.04	0.23	2.80	0.08	0.28	0.752	0.008	0.077
CS 22953-003	3.36	1.01	1.31	26.8	8.02	33.2	16.2	4.39	19.6	0.783	0.009	0.075
CS 22958-052	1.92	0.10	0.10	11.0	0.31	0.34	1.34	0.06	0.07	0.703	0.021	0.021
SMSS J024858.41−684306.4	5.71	0.62	0.44	434	138	140	151	53.0	60.9	0.974	0.015	0.008
HE 2327−5642	3.02	0.21	0.64	23.0	8.07	31.8	16.9	3.89	21.2	0.770	0.168	0.129
CS 29491-069	6.89	0.03	0.07	62.9	15.2	34.6	48.5	9.59	22.1	0.803	0.054	0.064
SMSS J051008.62−372019.8	6.04	0.14	0.18	9.93	0.07	0.07	7.71	0.17	0.16	0.244	0.017	0.013
BD +17°3248	0.13	0.08	0.11	7.74	0.00	0.00	3.43	2.06	0.09	0.967	0.027	0.021
CS 29529-054	0.56	0.03	0.02	8.96	0.08	0.13	3.63	1.87	0.04	0.884	0.006	0.005
J15582962−1224344	4.47	0.21	0.16	6.31	0.28	0.26	3.02	0.14	0.17	0.173	0.004	0.004
J00405260−5122491	0.13	0.03	0.02	8.12	0.01	0.08	1.05	0.01	0.02	0.969	0.004	0.007
CS 22943-132	5.43	0.03	0.03	9.41	0.07	0.08	4.65	0.14	0.15	0.268	0.006	0.007
CS 22896-154	4.93	1.41	0.48	6.05	0.21	2.76	1.78	0.25	1.40	0.184	0.114	0.172
HD 115444	1.05	0.12	0.11	11.0	0.18	0.20	1.43	0.10	0.12	0.826	0.020	0.020
HD 20	0.19	0.02	0.04	14.7	0.38	0.43	1.34	0.02	0.01	0.975	0.004	0.002
HD 221170	2.26	0.01	0.02	10.1	0.08	0.06	0.93	0.07	0.10	0.634	0.005	0.003
HE 0420+0123a	1.61	0.13	0.18	9.57	0.06	0.10	6.10	0.51	0.57	0.713	0.030	0.021
J19232518−5833410	1.04	0.52	0.66	8.57	0.14	0.29	5.40	0.67	0.62	0.784	0.105	0.100
HE 1430+0053	3.73	1.11	0.93	12.0	2.26	6.89	6.86	1.36	4.39	0.555	0.024	0.088
J01530024−3417360	0.38	0.06	0.05	11.9	0.12	0.13	0.69	0.02	0.02	0.938	0.008	0.008
J15271353−2336177	1.75	0.02	0.02	8.23	0.00	0.00	1.08	0.01	0.01	0.648	0.003	0.004

Note. The − and + columns indicate the 16th percentile and 84th percentile confidence intervals.

[Eu/Fe] = +1.00; Jacobson et al. 2015), is only loosely bound to the Milky Way. Its orbital properties lie well beyond several of the axes shown in Figure 4, with $r_{\mathrm{apo}} = 434^{+140}_{-138}$ kpc and $Z_{\mathrm{max}} = 151^{+61}_{-53}$ kpc. This orbit extends well beyond the Milky Way virial radius (≈280 kpc; Bland-Hawthorn & Gerhard 2016), and it may be on its first infall. Another star, CS 29491-069 ([Fe/H] = −2.55, [Eu/H] = −1.59, [Eu/Fe] = +0.96; Hayek et al. 2009), also has orbital properties too large for Figure 4, with $r_{\mathrm{apo}} = 63^{+35}_{-15}$ kpc and $Z_{\mathrm{max}} = 48^{+22}_{-10}$ kpc. While our work was in the final stages of preparation, Hawkins & Wyse (2018) presented an abundance analysis of several high-velocity stars, including two stars with [Eu/Fe] $\geqslant +0.7$ that appear to have *r*-process signatures. The kinematics of one of these stars, *Gaia* DR2 2233912206910720000 ([Fe/H] = −1.72, [Eu/H] = −0.61, [Eu/Fe] = +1.11), were examined by Hattori et al. (2018b), who found that it has only a 16% chance of being bound to the Milky Way. Whether or not it is bound, it has a high eccentricity and travels several hundred kiloparsecs from the Galactic center. High levels of *r*-process enhancement may be found in stars formed with a wide range of initial separations from the Milky Way, not just those that formed in the inner regions of the halo.

5.2. Clustering Analysis

In this section we investigate whether any subsets of highly *r*-process-enhanced stars could have formed together in individual satellites that were subsequently disrupted by the Milky Way. Simulations of satellite disruption indicate that structure remains in phase space after many Gyr of evolution (Helmi & de Zeeuw 2000; Font et al. 2006; Gómez et al. 2010). This structure may be distinguished in a Lindblad diagram (E versus L_z, the z component of the angular momentum), despite the fact that individual particles would be smoothly distributed across the sky when viewed from the solar neighborhood. Particles from an individual satellite are not single-valued in E or L_z, but they exhibit a small, characteristic spread (e.g., Figure 4 of Gómez et al.). Jean-Baptiste et al. (2017) raised concerns about using kinematics as the only tracer of structure in phase space, because multiple structures can overlap. Furthermore, structure may not be uniquely identified with an accreted component in galaxies with active merger histories and relatively massive companions with small pericentric radii. The Milky Way's merger history is not so active, and our study alleviates these concerns using a chemically selected sample.

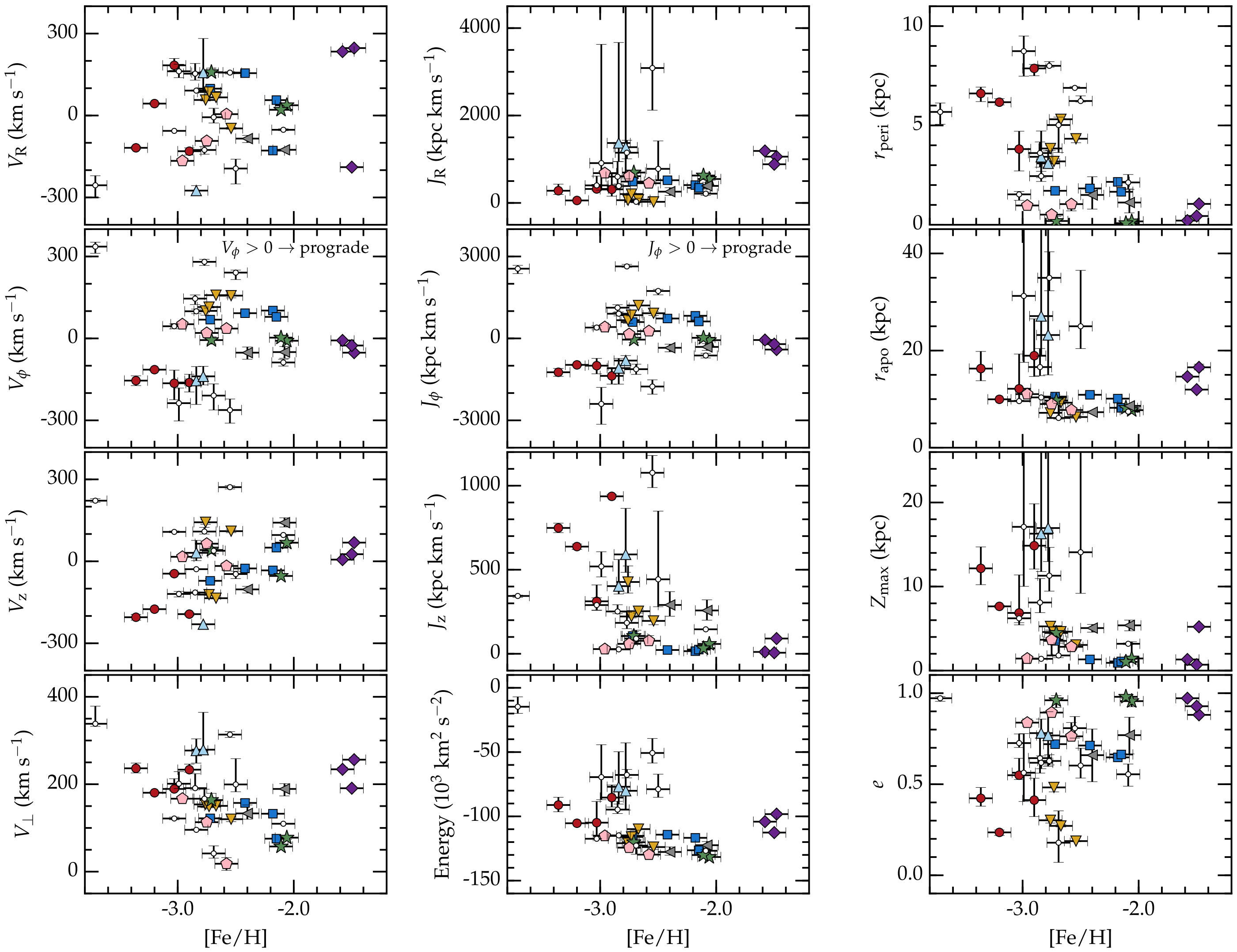

Figure 4. Calculated orbital and kinematic properties of groups of field *r*-process-enhanced stars as functions of [Fe/H]. Each group of stars is indicated by a different symbol/color combination, as shown in Figure 8 and discussed in Section 5.2. The error bars on the orbital and kinematic quantities represent the 16th and 84th percentiles of the distributions, and the error bars on [Fe/H] show a representative typical 0.10 dex uncertainty.

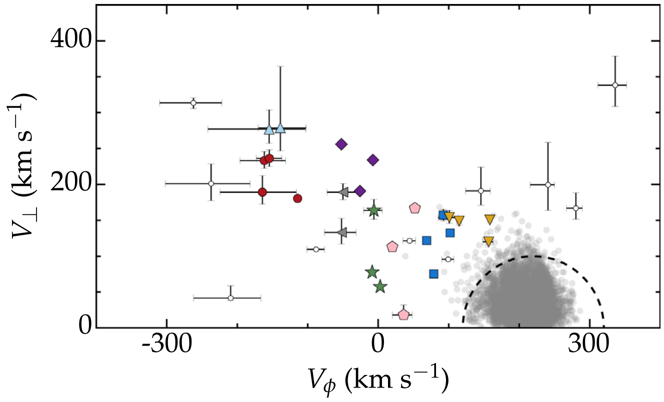

Figure 5. Toomre diagram in cylindrical coordinates for our sample of 35 highly *r*-process-enhanced stars. The cloud of gray circles centered near $V_\phi \approx 220$ km s^{-1} is a collection of 10,385 disk stars located within 200 pc of the Sun with $-0.25 <$ [Fe/H] $< +0.25$. The dashed line represents a total space velocity of 100 km s^{-1} relative to the local standard of rest in the V_ϕ direction. Each group of stars is indicated by a different symbol/color combination, as shown in Figure 8 and discussed in Section 5.2.

We search for structure among the highly *r*-process-enhanced stars in our sample using energy (E) and actions (J_r, J_ϕ, J_z). Energy is conserved as long as the potential of the Milky Way is static, and Gómez et al. (2010) showed that stars stripped from the same satellite remain clumped in E even in a realistic time-dependent potential. The actions are insensitive to the slow, adiabatic time-dependence of the potential. The azimuthal action J_ϕ ($=-L_z$) is conserved even if the potential is rapidly changing, as long as the potential remains axisymmetric.

We apply four clustering methods using the implementation from the `scikit-learn` python package: K-means (Lloyd 1982; Arthur & Vassilvitskii 2007), agglomerative (Ward 1963), affinity propagation (Frey & Dueck 2007), and mean-shift clustering (Comaniciu & Meer 2002). All four methods automatically assign each star to be a member of a cluster, although a cluster may consist of only one star. We adjust the clustering parameter values (number of clusters to be found, metric to be minimized, etc.) so that the resulting clusters appear reasonably coherent. Quantitative evaluations

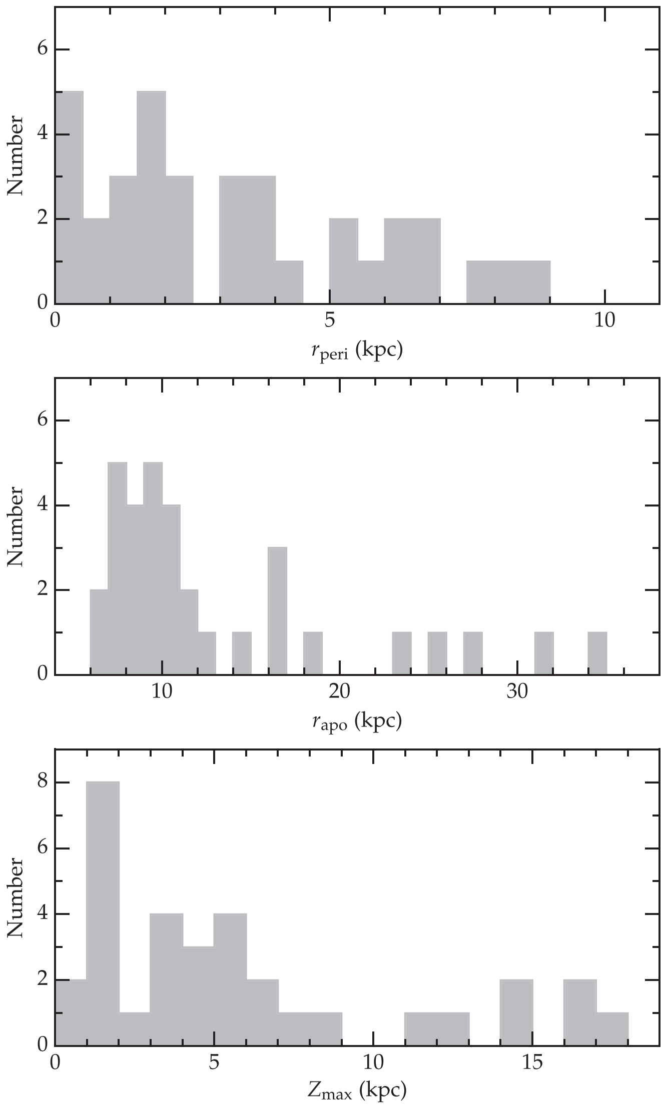

Figure 6. Histograms of the pericentric radii (top), apocentric radii (middle), and maximum distance above or below the Galactic plane (bottom) for the 35 highly *r*-process-enhanced stars in our sample. Note that two stars with large $r_{\rm apo}$ (63^{+35}_{-15} kpc and 434^{+140}_{-138} kpc) and $Z_{\rm max}$ (48^{+22}_{-10} kpc and 151^{+61}_{-53} kpc) are not shown in the middle and bottom panels.

of the clusters (the silhouette coefficient, Rousseeuw 1987; or the Calinski–Harabasz Index, Calinski & Harabasz 1974) fail to distinguish precise values for the number of clusters or other parameters beyond general ranges. Typically, ≈8–12 clusters are preferred, including single-star clusters. We test the reproducibility of these clustering methods by repeatedly drawing from the input error distributions and recomputing the clusters. The K-means method is highly sensitive to these draws, resulting in unstable cluster membership from one draw to another, so we discard the K-means method from further consideration. The other three methods are stable against the input draws, with only 1–2 stars changing cluster membership <10% of the time.

Figure 7 illustrates our adopted clustering results from the three methods. Only the relationship between E and J_ϕ is shown, although the clustering has been performed for E, J_r, J_ϕ, and J_z. Each set of symbols in each panel represents one cluster. A few points are worth mentioning. First, the stars with lower values of E overlap more than stars with higher E, so cluster definitions are more challenging in this region of the diagram. Second, there are relatively few stars with high E values, so these stars are commonly identified as the single members of their clusters. Third, although the membership of individual clusters differs from one method to another, some subsets of stars are always grouped together.

We associate 25 of the 35 stars into 8 groups for which the three clustering methods all agree. These groups range in membership from two to four stars each, and they are illustrated in Figures 4 and 8 and listed in Table 6. We assert that the cluster candidates illustrated in Figure 8 offer a more representative, conservative expression of the data than the results of any individual clustering method. The behavior of the candidate clusters resembles the extended structures in E and J_ϕ (or L_z) predicted by simulations, as shown in Figure 4 of Gómez et al. (2010). The 10 stars that could not be conclusively assigned to these groups are shown as small white circles in Figure 8.

5.3. Evaluating the Groups Using Stellar Abundances

No chemical information is considered in the clustering process, so the stellar abundances can be used to evaluate group membership. Visual inspection of Figure 4 suggests that the groups span a small range of [Fe/H] values relative to the full sample of 35 stars (≈2.2 dex). The group [Fe/H] ranges span 0.10–0.65 dex with dispersions 0.04–0.30 dex. For comparison, the seven highly *r*-process-enhanced stars in Ret II whose abundances have been studied span a range in [Fe/H] of 0.93 dex with a dispersion of 0.35 dex (Ji et al. 2016b). The typical statistical (systematic) uncertainties of [Fe/H] ratios are ≈0.1 (0.2) dex, so the smallest group [Fe/H] dispersions may represent upper limits. The small dispersions could signal that our groups represent remnants of individual dwarf galaxies with moderate spreads in [Fe/H].

We check the significance of the small [Fe/H] dispersions for stars within each group as follows. We draw 4 [Fe/H] values at random, without replacement, from the 35 stars and compute the sample standard deviation. We repeat this process 10^5 times and compute the probability density distribution. Figure 9 illustrates the results of this test. The top panel indicates the [Fe/H] dispersions for the stars in groups A, B, and C, each of which contain four stars. The bottom panel of Figure 9 illustrates the results of an analogous test where three [Fe/H] values are drawn at random, and these results are compared with the [Fe/H] dispersions for the stars in groups D, E, and F, each of which contain three stars. All six groups have smaller [Fe/H] dispersions than the median expected dispersion, and the dispersions in groups A–F are smaller than that of randomly selected stars in 80.8%, 87.9%, 98.1%, 98.0%, 55.6%, and 80.9% of cases, respectively. The dispersion in [Eu/H] is also small for many of these groups, and a similar analysis reveals that it is smaller than that of randomly selected stars in 99.3%, 29.7%, 93.5%, 54.2%, 74.3%, and 63.6% of cases for groups A–F, respectively. We regard this result as evidence that at least some of these groups are legitimate, and we proceed under this assumption as a starting point for investigation. Additional tests of the legitimacy of these groups, such as searches for more *r*-process-enhanced stars with similar kinematics or revisiting the clustering analysis using a range of Milky Way potentials, would be most welcome.

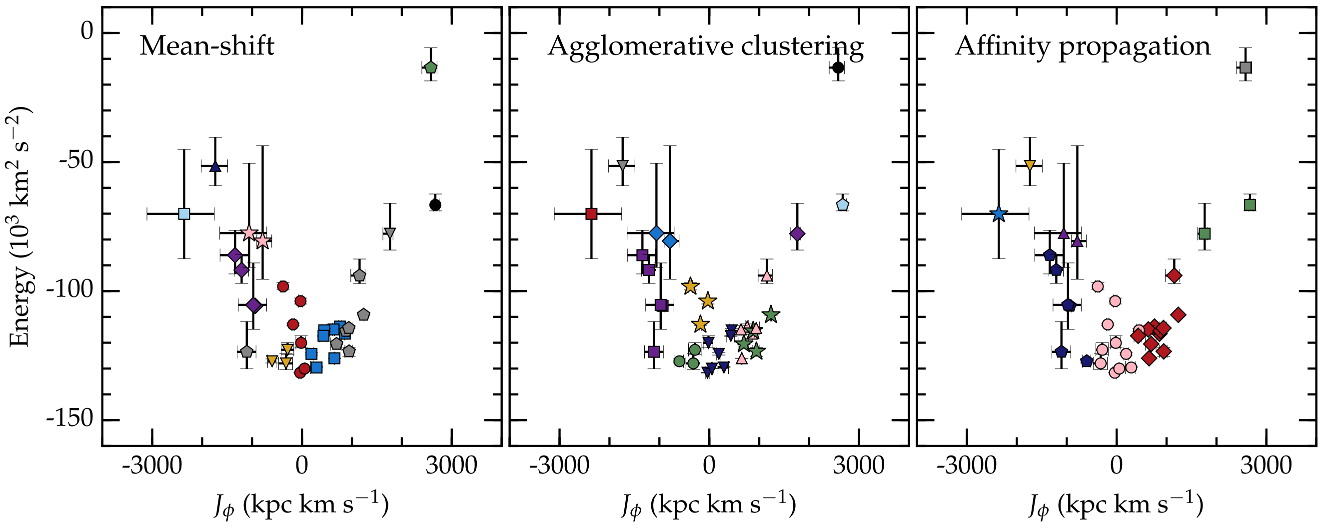

Figure 7. Results of three different clustering methods applied to the 35 stars in our sample. Different symbol shapes and colors in each panel indicate the different groups. Each symbol shape and color is only used in a single panel, and these combinations are not used in other figures. The error bars represent the 16th and 84th percentiles of the distributions. Only the relationship between E and J_ϕ is shown, even though the clustering has been performed over four dimensions (E, J_r, J_ϕ, and J_z).

5.4. The Environment of the r-process

Environmental constraints on the *r*-process have been derived from the ultra-faint dwarf galaxy Ret II (e.g., Beniamini et al. 2016; Ji et al. 2016a; Safarzadeh & Scannapieco 2017) and chemical evolution models of the Milky Way (e.g., Cescutti et al. 2015; Ishimaru et al. 2015; Shen et al. 2015; Côté et al. 2018; and references therein). Astrometry from the *Gaia* satellite now enables similar constraints to be derived from stars in the solar neighborhood. The highly *r*-process-enhanced field stars in our sample may be in situ halo stars, disk or bulge stars ejected into halo orbits, or accreted from satellites. A population of stars ejected from the disk would retain a net prograde rotation. The net rotation of our sample is consistent with zero (Section 5.1), so it is unlikely that our sample is dominated by stars ejected from the disk. An accretion origin is likely for the stars with large orbital apocenters or retrograde orbits. In situ or ejected stars are less likely to exhibit structure in both phase space and metallicity, so the groups identified in Section 5.2 also favor the accretion scenario. The 25 stars in groups and the 7 unaffiliated stars with $r_{\rm apo} > 20$ kpc or $V_\phi < 0$ km s^{-1} constitute the majority (91%) of the sample, so most if not all of these highly *r*-process enhanced stars were likely accreted.

The metallicity range of our sample ([Fe/H] < -1.4) overlaps with the metal-poor end of the Milky Way disk. A sizable number of stars with [Fe/H] at least as low as -2, and possibly lower, are found on disk-like orbits (e.g., Ruchti et al. 2011; Kordopatis et al. 2013; Beers et al. 2014). Many of the known highly *r*-process-enhanced stars were identified in non-kinematically selected surveys, and Beers et al. (2000) and Chiba & Beers (2000) confirm that these surveys contain metal-poor disk and halo stars. If the occurrence frequency of highly *r*-process-enhanced stars is only a function of [Fe/H], then such stars should also be found among the disk populations. We find no evidence in our data to support this assertion. Increasing the number of highly *r*-process-enhanced stars with [Fe/H] > -2 with well-determined distances and kinematics would help to strengthen this conclusion.

Many *r*-process events have occurred in the Milky Way disk, bulge, and globular clusters. This fact is evident from the observation that stars in these populations contain substantial amounts of *r*-process material ([Eu/H] > -1.5), comparable to the most highly *r*-process-enhanced stars in our sample. The [Eu/Fe] ratios in disk, bulge, and globular cluster stars are different, however, in that they rarely exceed [Eu/Fe] $\approx +0.6$ (e.g., Gratton et al. 2004; Johnson et al. 2012; Battistini & Bensby 2016). This observation suggests that the difference between these populations and the halo stars we have identified may be the timescales of producing Fe. Consequently, environments with lower star formation efficiencies that produce less Fe, like dwarf galaxies, may be necessary to produce extreme ([Eu/Fe] $\geqslant +0.7$) *r*-process enhancement. This conclusion suggests that the key to obtaining highly *r*-process-enhanced stars may be the environment where the *r*-process occurs, not the nature of its site. A single site, such as neutron-star mergers, could dominate *r*-process production in all environments.

5.5. The Nature of the Progenitor Satellites

The kinematics and abundances of the accreted stars in our sample also help reveal the nature of their progenitor satellites. Simulations by Wetzel (2011) and van den Bosch et al. (2016) find that satellites accreted at higher redshifts are more radial, have smaller orbital radii, and are more tightly bound to the host than those accreted at lower redshifts. The simulations of Rocha et al. (2012) revealed that the satellites with the earliest infall times were the most tightly bound at $z = 0$. Rocha et al. anticipated that a similar relation for tidal streams could exist, although dynamical friction can complicate this simple picture (see also Amorisco 2017). The orbital pericenters of all stars in our sample are much smaller than that of Ret II (29^{+4}_{-6} kpc, Simon 2018; 20 ± 5 kpc, Fritz et al. 2018) and most of the

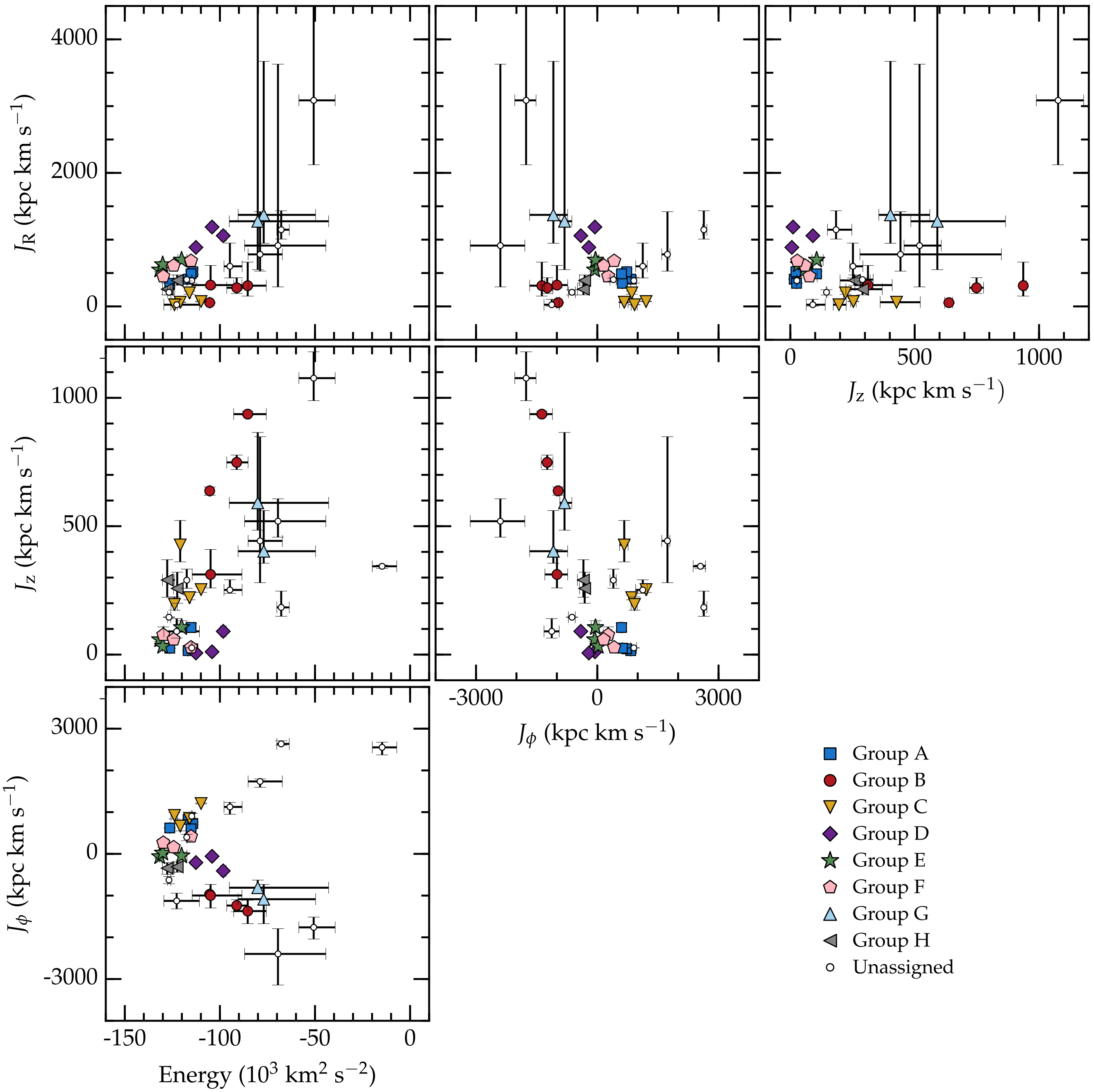

Figure 8. Groups of field *r*-process-enhanced stars as functions of E, J_r, J_ϕ, and J_z. Each group of stars is indicated by a different symbol/color combination, as indicated in the legend. The small white circles indicate stars that were not conclusively associated with one of these groups, either because their membership was ambiguous or because they are outliers. The error bars represent the 16th and 84th percentiles of the distributions for each quantity.

surviving low-mass dwarf galaxies, whose orbital pericenters are located ∼10–100 kpc from the Galactic center (Fritz et al.). Many of the highly *r*-process-enhanced stars in our sample likely originated in progenitor systems with small pericentric radii that caused them to disrupt much earlier than the surviving dwarf galaxies.

The similarity between the [Eu/Fe] and [Eu/H] ratios found in Ret II and highly *r*-process-enhanced field stars (Figure 1) suggests a common mass scale between lower-mass dwarf galaxies and the progenitor satellites of highly *r*-process-enhanced field stars. Seven of the eight groups we have identified have mean metallicities $-3.2 < \mathrm{[Fe/H]} < -2.2$, as illustrated in Figure 10. If these metallicities are representative of the progenitor systems, then the galaxy luminosity–metallicity relation predicts satellite progenitors with $M_V \gtrsim -9$ or $\log L \lesssim 5.5$ (Kirby et al. 2008; Walker et al. 2016). This scale includes ultra-faint dwarf galaxies, like Ret II, and low-luminosity classical dwarf spheroidal galaxies, like Dra and UMi, which are also known to host a handful of highly *r*-process-enhanced stars (Shetrone et al. 2001; Aoki et al. 2007; Cohen & Huang 2009, 2010; Tsujimoto et al. 2017).

It seems unlikely that the high level of *r*-process enhancement in group D stars would be found in all stars in a

Table 6
Groups of *r*-process-enhanced Field Stars

Group	Members	[Fe/H]	[Eu/Fe]	[Eu/H]
A	HE 0430−4901	−2.72	+1.16	−1.56
	CS 22958-052	−2.42	+1.00	−1.42
	HD 221170	−2.18	+0.80	−1.38
	J15271353−2336177	−2.15	+0.70	−1.45
B	J235718.91−005247.8	−3.36	+1.92	−1.44
	CS 31082-001	−2.90	+1.63	−1.27
	SMSS J051008.62−372019.8	−3.20	+0.95	−2.25
	HE 1430+0053	−3.03	+0.72	−2.31
C	J21064294−6828266	−2.76	+1.32	−1.44
	CS 22945-017	−2.73	+1.13	−1.60
	J15582962−1224344	−2.54	+0.89	−1.65
	CS 22943-132	−2.67	+0.86	−1.81
D	HD 222925	−1.47	+1.33	−0.14
	HD 20	−1.58	+0.80	−0.78
	J01530024−3417360	−1.50	+0.71	−0.79
E	CS 22945-058	−2.71	+1.13	−1.58
	BD +17°3248	−2.06	+0.91	−1.15
	J00405260−5122491	−2.11	+0.86	−1.25
F	HE 2224+0143	−2.58	+1.05	−1.53
	CS 29529-054	−2.75	+0.90	−1.85
	HD 115444	−2.96	+0.85	−2.11
G	CS 22953-003	−2.84	+1.05	−1.79
	HE 2327−5642	−2.78	+0.98	−1.80
H	J21091825−1310062	−2.40	+1.25	−1.15
	J19232518−5833410	−2.08	+0.76	−1.32

progenitor of mass comparable to Scl ($M_* \approx 2.3 \times 10^6\ M_\odot$; McConnachie 2012), because few known field *r*-process-enhanced stars have such high metallicities. The small metallicity dispersion of group D is reminiscent of a globular cluster, but the stars in group D do not exhibit the light-element chemical signatures in O, Na, or Al that are found in some globular cluster populations (Barklem et al. 2005; Roederer et al. 2014b, 2018). We speculate that the stars in group D may have formed in a relatively dense clump of gas in close proximity to an *r*-process event in the progenitor system.

We also estimate the initial stellar mass of these systems using the [Eu/H] ratios and theoretical *r*-process yields from neutron-star mergers. The total stellar mass, M_*, is given by

$$M_* = \varepsilon_{\rm SF}\, M_{r,\rm ej}\, f_{r,\rm Eu}\, A_{\rm Eu}^{-1}\, f_{\rm keep}\, 10^{12-[\rm Eu/H]}. \qquad (2)$$

We assume that the *r*-process material is diluted into H, but only some fraction of this gas will be converted into stars. Here, $\varepsilon_{\rm SF}$ is the star formation efficiency, defined from 0 to 1 as the fraction of gas converted to stars. This value is expected to be low in satellites found in low-mass halos (Behroozi et al. 2013), and we adopt $\varepsilon_{\rm SF} = 0.01$. $M_{r,\rm ej}$ is the mass in $M_\odot$ of *r*-process material ejected. For a neutron-star merger, $M_{r,\rm ej} \sim 0.005\ M_\odot$, which is the yield of dynamical wind ejecta with low electron fractions (Y_e) that will produce nuclei at and between the second and third *r*-process peaks, including Eu (see Côté et al. 2018, and references therein). The term $f_{r,\rm Eu}$ represents the mass fraction of Eu among the *r*-process material, which is ≈0.006 by mass for nuclei at and beyond the second *r*-process peak ($Z \geqslant 52$; cf. Roederer et al. 2012a) when adopting the solar *r*-process residuals (Sneden et al. 2008). $A_{\rm Eu}$ is the average mass of Eu in atomic mass units, which is ≈152 for the Eu isotopic ratios found in the Sun and *r*-process-enhanced metal-poor stars (e.g., Sneden et al. 2002). The term $f_{\rm keep}$ is the fraction of *r*-process material retained by the system, which depends on factors like the location of the event within the satellite's potential well (Safarzadeh & Scannapieco 2017). We adopt $f_{\rm keep} = 1$ (Beniamini et al. 2018). [Eu/H] is the average stellar abundance ratio for each group.

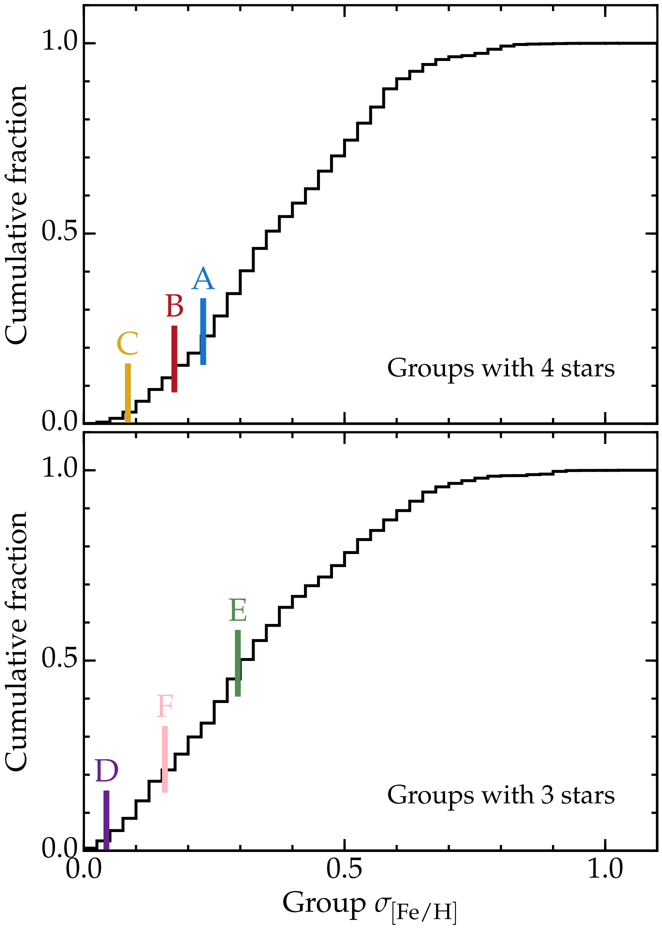

Figure 9. Comparison of the [Fe/H] dispersion ($\sigma_{\rm [Fe/H]}$) for groups A, B, C, D, E, and F with cumulative probability density distributions for the sample standard deviation of random draws of [Fe/H] from our sample of 35 stars. The top panel shows the results of drawing four [Fe/H] values, and the bottom panel shows the results of drawing three [Fe/H] values. For comparison, the [Fe/H] dispersion in Ret II is 0.35 dex.

Our calculation makes several simplifying assumptions. We assume that all stars formed after the injection of *r*-process material, which is a reasonable approximation for the fraction of stars that are *r*-process-enhanced in Ret II, but it cannot be strictly correct. We calculate M_* values at the time of star formation, and these values would be smaller by $\lesssim$40% today because stars with $M \gtrsim 0.8\,M_\odot$ have evolved and lost a substantial fraction of their initial mass. We ignore this small correction when comparing the initial stellar masses of the satellite progenitors with the masses of present-day dwarf galaxies. Under these assumptions, the mean [Eu/H] ratios in

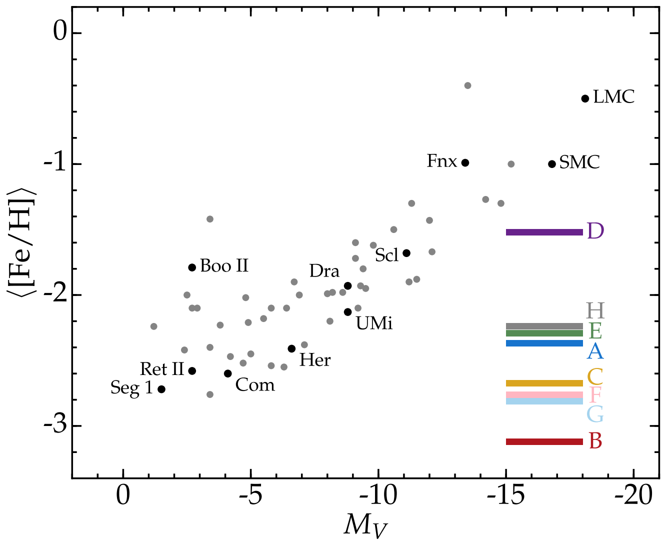

Figure 10. Comparison of the mean metallicities of groups A–H with the galaxy luminosity–metallicity relation for Local Group galaxies. Only galaxies with spectroscopically determined mean metallicities are shown. The names of a few representative galaxies are indicated. The data for the Local Group galaxies are adopted from McConnachie (2012), Kirby et al. (2015, 2017a, 2017b), Koposov et al. (2015a, 2015b, 2018), Laevens et al. (2015), Martin et al. (2015, 2016), Walker et al. (2015, 2016), Kim et al. (2016), Caldwell et al. (2017), Carlin et al. (2017), Li et al. (2017), Simon et al. (2017), and Torrealba et al. (2018).

the eight groups predict $M_* \sim 0.7$–$10 \times 10^4\,M_\odot$. These masses are comparable to the stellar masses of ultra-faint dwarf galaxies, like Com ($M_* \approx 7 \times 10^3\,M_\odot$) or Her ($M_* \approx 5 \times 10^4\,M_\odot$; Martin et al. 2008). These order-of-magnitude mass estimates match those from the luminosity–metallicity relation.

6. Conclusions

Traditional chemical tagging relies on the existence of chemically homogeneous populations of stars (e.g., Freeman & Bland-Hawthorn 2002). We instead use field stars that are highly enhanced in *r*-process elements ([Eu/Fe] $\geqslant +0.7$) to characterize the environments where the *r*-process occurred. We examine the three-dimensional velocities, integrals of motion, energy, and orbits of 35 highly *r*-process-enhanced stars with parallax errors <12.5% in the *Gaia* DR2 catalog.

More than 77% of the 35 highly *r*-process-enhanced stars are on eccentric ($e > 0.5$), radial orbits. About 66% of the stars are on orbits that remain within the inner regions of the halo (<13 kpc), and more than 51% of the stars pass within 2.6 kpc of the Galactic center. At the other extreme, 20% of the stars have orbital apocenters >20 kpc, including one star (SMSS J024858.41−684306.4) whose orbital apocenter is larger than the Milky Way virial radius. None of the stars have disk-like kinematics, despite the fact that the metal-rich end of our sample overlaps with the metal-poor end of the disk. Roughly equal numbers of stars are moving radially inward and outward, north and south, and prograde and retrograde, indicating that a substantial amount of phase-mixing has occurred.

We identify eight candidate kinematic groups of field *r*-process-enhanced stars based on structure in their orbital energies and integrals of motion. These groups show smaller [Fe/H] (and sometimes [Eu/H]) dispersion than would be expected by random chance. The orbital properties, clustering in phase space, and lack of highly *r*-process-enhanced stars on disk-like orbits indicate that many, if not all, highly *r*-process-enhanced field stars originated in satellites that were later disrupted by the Milky Way. The dwarf galaxy luminosity–metallicity relation predicts satellite progenitors with $M_V \gtrsim -9$ or $\log L \lesssim 5.5$ based on the low mean metallicities of seven of the eight groups. Theoretical *r*-process yields of neutron-star mergers and the stellar [Eu/H] ratios predict stellar masses $\sim$0.6–10 $\times$ $10^4\,M_\odot$ for the progenitor systems when a number of simplifying assumptions are made. These scales favor ultra-faint dwarf galaxies or low-luminosity dwarf spheroidal galaxies as the birthplaces of highly *r*-process-enhanced stars.

Comparable levels of *r*-process enhancement ([Eu/H] > -1.5) are found in the *r*-process-enhanced field stars and disk and globular cluster populations, but stars with [Eu/Fe] $\geqslant +0.7$ are only found among stars with halo orbits. This observation suggests that [Eu/Fe] $\geqslant +0.7$ may represent a more natural lower limit for classifying highly *r*-process-enhanced stars. We suggest that the distinguishing factor may be the different rates of Fe production. Environments with lower star formation efficiency, like dwarf galaxies, may be necessary to obtain extreme ([Eu/Fe] $\geqslant +0.7$) *r*-process enhancement in subsequent stellar generations. This conclusion allows for the possibility that a single site, like neutron-star mergers, could dominate *r*-process production in all environments.

The significance of our conclusions can be assessed by future work. Our study is limited by the small number of highly *r*-process-enhanced stars with reliable kinematics available at present. Efforts like the *R*-Process Alliance will identify much larger samples of such stars in the near future, and these larger samples will help to confirm or reject the conclusions of our work.

We thank the referee for providing useful suggestions and members of the stellar halos group at the University of Michigan for stimulating discussions. I.U.R. thanks T. Beers, E. Bell, B. Côté, G. Cescutti, and A. Ji for comments on earlier versions of the manuscript. K.H. thanks E. Vasiliev for making Galactic Dynamics code `Agama` publicly available. I.U.R. acknowledges support from grants AST 16-13536, AST 18-15403, and PHY 14-30152 (Physics Frontier Center/JINA-CEE) awarded by the U.S. National Science Foundation (NSF). K.H. and M.V. are supported by NASA-ATP award NNX15AK79G (PI: M. Valluri). This research has made use of NASA's Astrophysics Data System Bibliographic Services; the arXiv pre-print server operated by Cornell University; the SIMBAD and VizieR databases hosted by the Strasbourg Astronomical Data Center; and the JINAbase database (Abohalima & Frebel 2017). This work has also made use of data from the European Space Agency (ESA) mission *Gaia* (http://www.cosmos.esa.int/gaia), processed by the *Gaia* Data Processing and Analysis Consortium (DPAC, http://www.cosmos.esa.int/web/gaia/dpac/consortium). Funding for the DPAC has been provided by national institutions, in particular the institutions participating in the *Gaia* Multilateral Agreement. Funding for RAVE has been provided by: the Australian Astronomical Observatory; the Leibniz-Institut fuer Astrophysik Potsdam (AIP); the Australian National University; the Australian Research Council; the French National Research Agency; the German Research Foundation (SPP 1177 and SFB

881); the European Research Council (ERC-StG 240271 Galactica); the Istituto Nazionale di Astrofisica at Padova; The Johns Hopkins University; the U.S. N.S.F. (AST-0908326); the W.M. Keck foundation; the Macquarie University; the Netherlands Research School for Astronomy; the Natural Sciences and Engineering Research Council of Canada; the Slovenian Research Agency; the Swiss National Science Foundation; the Science & Technology Facilities Council of the UK; Opticon; Strasbourg Observatory; and the Universities of Groningen, Heidelberg and Sydney.

Facility: Gaia.

Software: Agama (Vasiliev 2018), matplotlib (Hunter 2007), numpy (van der Walt et al. 2011), scikit-learn (Pedregosa et al. 2011), scipy (Jones et al. 2001).

ORCID iDs

Ian U. Roederer https://orcid.org/0000-0001-5107-8930
Kohei Hattori https://orcid.org/0000-0001-6924-8862
Monica Valluri https://orcid.org/0000-0002-6257-2341

References

Abbott, B. P., Abbott, R., Abbott, T. D., et al. 2017a, PhRvL, 119, 161101
Abbott, B. P., Abbott, R., Abbott, T. D., et al. 2017b, ApJL, 848, L12
Abohalima, A., & Frebel, A. 2017, arXiv:1711.04410
Afşar, M., Sneden, C., Frebel, A., et al. 2016, ApJ, 819, 103
Amorisco, N. C. 2017, MNRAS, 464, 2882
Aoki, W., Beers, T. C., Honda, S., & Carollo, D. 2010, ApJL, 723, L201
Aoki, W., Honda, S., Sadakane, K., & Arimoto, N. 2007, PASJ, 59, L15
Arthur, D., & Vassilvitskii, S. 2007, in Proc. Eighteenth Annual ACM-SIAM Symp. Discrete Algorithms, SODA '07, ed. H. Gabow (Philadelphia, PA: Society for Industrial and Applied Mathematics), 1027
Bailer-Jones, C. A. L., Rybizki, J., Fouesneau, M., Mantelet, G., & Andrae, R. 2018, AJ, 156, 58
Barklem, P. S., Christlieb, N., Beers, T. C., et al. 2005, A&A, 439, 129
Battistini, C., & Bensby, T. 2016, A&A, 586, A49
Beers, T. C., Chiba, M., Yoshii, Y., et al. 2000, AJ, 119, 2866
Beers, T. C., & Christlieb, N. 2005, ARA&A, 43, 531
Beers, T. C., Norris, J. E., Placco, V. M., et al. 2014, ApJ, 794, 58
Beers, T. C., Preston, G. W., & Shectman, S. A. 1985, AJ, 90, 2089
Beers, T. C., Preston, G. W., & Shectman, S. A. 1992, AJ, 103, 1987
Behr, B. B. 2003, ApJS, 149, 101
Behroozi, P. S., Wechsler, R. H., & Conroy, C. 2013, ApJL, 762, L31
Beniamini, P., Dvorkin, I., & Silk, J. 2018, MNRAS, 478, 1994
Beniamini, P., Hotokezaka, K., & Piran, T. 2016, ApJ, 832, 149
Bidelman, W. P., & MacConnell, D. J. 1973, AJ, 78, 687
Binney, J. 2012, MNRAS, 426, 1324
Bisterzo, S., Gallino, R., Straniero, O., Cristallo, S., & Käppeler, F. 2011, MNRAS, 418, 284
Bland-Hawthorn, J., & Gerhard, O. 2016, ARA&A, 54, 529
Bond, H. E. 1980, ApJS, 44, 517
Bonifacio, P., Spite, M., Cayrel, R., et al. 2009, A&A, 501, 519
Bovy, J. 2015, ApJS, 216, 29
Bovy, J. 2017, MNRAS, 470, 1360
Caldwell, N., Walker, M. G., Mateo, M., et al. 2017, ApJ, 839, 20
Calinski, T., & Harabasz, J. 1974, Communications in Statistics, 3, 1
Carlin, J. L., Sand, D. J., Muñoz, R. R., et al. 2017, AJ, 154, 267
Cescutti, G., Romano, D., Matteucci, F., Chiappini, C., & Hirschi, R. 2015, A&A, 577, A139
Chiba, M., & Beers, T. C. 2000, AJ, 119, 2843
Christlieb, N., Schörck, T., Frebel, A., et al. 2008, A&A, 484, 721
Cohen, J. G., Christlieb, N., Thompson, I., et al. 2013, ApJ, 778, 56
Cohen, J. G., & Huang, W. 2009, ApJ, 701, 1053
Cohen, J. G., & Huang, W. 2010, ApJ, 719, 931
Comaniciu, D., & Meer, P. 2002, ITPAM, 24, 603
Côté, B., Fryer, C. L., Belczynski, K., et al. 2018, ApJ, 855, 99
Cowan, J. J., Sneden, C., Burles, S., et al. 2002, ApJ, 572, 861
Cowperthwaite, P. S., Berger, E., Villar, V. A., et al. 2017, ApJL, 848, L17
Dotter, A., Chaboyer, B., Jevremović, D., et al. 2008, ApJS, 178, 89
Drout, M. R., Piro, A. L., Shappee, B. J., et al. 2017, Sci, 358, 1570
Font, A. S., Johnston, K. V., Bullock, J. S., & Robertson, B. E. 2006, ApJ, 646, 886
François, P., Depagne, E., Hill, V., et al. 2007, A&A, 476, 935
Frebel, A., Christlieb, N., Norris, J. E., et al. 2007, ApJL, 660, L117
Freeman, K., & Bland-Hawthorn, J. 2002, ARA&A, 40, 487
Frey, B. J., & Dueck, D. 2007, Sci, 315, 972
Fritz, T. K., Battaglia, G., Pawlowski, M. S., et al. 2018, arXiv:1805.00908
Gilroy, K. K., Sneden, C., Pilachowski, C. A., & Cowan, J. J. 1988, ApJ, 327, 298
Gómez, F. A., Helmi, A., Brown, A. G. A., & Li, Y.-S. 2010, MNRAS, 408, 935
Gratton, R., Sneden, C., & Carretta, E. 2004, ARA&A, 42, 385
Hansen, T. T., Andersen, J., Nordström, B., et al. 2015, A&A, 583, A49
Hansen, T. T., Holmbeck, E. M., Beers, T. C., et al. 2018, ApJ, 858, 92
Hattori, K., Gouda, N., Yano, T., et al. 2018a, arXiv:1804.01920
Hattori, K., Valluri, M., Bell, E. F., & Roederer, I. U. 2018b, arXiv:1805.03194
Hawkins, K., & Wyse, R. F. G. 2018, MNRAS, 481, 1028
Hayek, W., Wiesendahl, U., Christlieb, N., et al. 2009, A&A, 504, 511
Helmi, A., & de Zeeuw, P. T. 2000, MNRAS, 319, 657
Hill, V., Christlieb, N., Beers, T. C., et al. 2017, A&A, 607, A91
Hill, V., Plez, B., Cayrel, R., et al. 2002, A&A, 387, 560
Hollek, J. K., Frebel, A., Roederer, I. U., et al. 2011, ApJ, 742, 54
Holmbeck, E. M., Beers, T. C., Roederer, I. U., et al. 2018, ApJL, 859, L24
Honda, S., Aoki, W., Kajino, T., et al. 2004, ApJ, 607, 474
Hotokezaka, K., Piran, T., & Paul, M. 2015, NatPh, 11, 1042
Howes, L. M., Asplund, M., Keller, S. C., et al. 2016, MNRAS, 460, 884
Howes, L. M., Casey, A. R., Asplund, M., et al. 2015, Natur, 527, 484
Hunter, J. D. 2007, CSE, 9, 90
Ishimaru, Y., Wanajo, S., & Prantzos, N. 2015, ApJL, 804, L35
Ivans, I. I., Simmerer, J., Sneden, C., et al. 2006, ApJ, 645, 613
Jacobson, H. R., Keller, S., Frebel, A., et al. 2015, ApJ, 807, 171
Jean-Baptiste, I., Di Matteo, P., Haywood, M., et al. 2017, A&A, 604, A106
Ji, A. P., Frebel, A., Chiti, A., & Simon, J. D. 2016a, Natur, 531, 610
Ji, A. P., Frebel, A., Simon, J. D., & Chiti, A. 2016b, ApJ, 830, 93
Johnson, C. I., McWilliam, A., & Rich, R. M. 2013, ApJL, 775, L27
Johnson, C. I., Rich, R. M., Kobayashi, C., & Fulbright, J. P. 2012, ApJ, 749, 175
Jones, E., Oliphant, T., Peterson, P., et al. 2001, SciPy: Open source scientific tools for Python, https://www.scipy.org/
Kasen, D., Metzger, B., Barnes, J., Quataert, E., & Ramirez-Ruiz, E. 2017, Natur, 551, 80
Kim, D., Jerjen, H., Geha, M., et al. 2016, ApJ, 833, 16
Kirby, E. N., Cohen, J. G., Simon, J. D., et al. 2017a, ApJ, 838, 83
Kirby, E. N., Rizzi, L., Held, E. V., et al. 2017b, ApJ, 834, 9
Kirby, E. N., Simon, J. D., & Cohen, J. G. 2015, ApJ, 810, 56
Kirby, E. N., Simon, J. D., Geha, M., Guhathakurta, P., & Frebel, A. 2008, ApJL, 685, L43
Koposov, S. E., Belokurov, V., Torrealba, G., & Evans, N. W. 2015a, ApJ, 805, 130
Koposov, S. E., Casey, A. R., Belokurov, V., et al. 2015b, ApJ, 811, 62
Koposov, S. E., Walker, M. G., Belokurov, V., et al. 2018, MNRAS, 479, 5343
Kordopatis, G., Gilmore, G., Wyse, R. F. G., et al. 2013, MNRAS, 436, 3231
Kunder, A., Kordopatis, G., Steinmetz, M., et al. 2017, AJ, 153, 75
Laevens, B. P. M., Martin, N. F., Bernard, E. J., et al. 2015, ApJ, 813, 44
Lai, D. K., Bolte, M., Johnson, J. A., et al. 2008, ApJ, 681, 1524
Li, T. S., Simon, J. D., Drlica-Wagner, A., et al. 2017, ApJ, 838, 8
Lindegren, L., Hernandez, J., Bombrun, A., et al. 2018, A&A, 616, A2
Lindegren, L., Lammers, U., Bastian, U., et al. 2016, A&A, 595, A4
Lloyd, S. P. 1982, ITIT, 28, 129
Martin, N. F., de Jong, J. T. A., & Rix, H.-W. 2008, ApJ, 684, 1075
Martin, N. F., Geha, M., Ibata, R. A., et al. 2016, MNRAS, 458, L59
Martin, N. F., Nidever, D. L., Besla, G., et al. 2015, ApJL, 804, L5
Mashonkina, L., Christlieb, N., Barklem, P. S., et al. 2010, A&A, 516, A46
Mashonkina, L., Christlieb, N., & Eriksson, K. 2014, A&A, 569, A43
McConnachie, A. W. 2012, AJ, 144, 4
Naiman, J. P., Pillepich, A., Springel, V., et al. 2018, MNRAS, 477, 1206
Pedregosa, F., Varoquaux, G., Gramfort, A., et al. 2011, Journal of Machine Learning Research, 12, 2825
Placco, V. M., Holmbeck, E. M., Frebel, A., et al. 2017, ApJ, 844, 18
Rocha, M., Peter, A. H. G., & Bullock, J. 2012, MNRAS, 425, 231
Roederer, I. U. 2009, AJ, 137, 272
Roederer, I. U., Cowan, J. J., Preston, G. W., et al. 2014a, MNRAS, 445, 2970
Roederer, I. U., Lawler, J. E., Cowan, J. J., et al. 2012a, ApJL, 747, L8
Roederer, I. U., Lawler, J. E., Sobeck, J. S., et al. 2012b, ApJS, 203, 27

Roederer, I. U., Mateo, M., Bailey, J. I., III, et al. 2016, AJ, 151, 82
Roederer, I. U., Preston, G. W., Thompson, I. B., et al. 2014b, AJ, 147, 136
Roederer, I. U., Sakari, C. M., Placco, V. M., et al. 2018, ApJ, in press, arXiv:1808.09469
Rousseeuw, P. J. 1987, JCoAM, 20, 53
Ruchti, G. R., Fulbright, J. P., Wyse, R. F. G., et al. 2011, ApJ, 737, 9
Safarzadeh, M., & Scannapieco, E. 2017, MNRAS, 471, 2088
Sakari, C. M., Placco, V. M., Hansen, T., et al. 2018, ApJL, 854, L20
Schönrich, R., Binney, J., & Dehnen, W. 2010, MNRAS, 403, 1829
Shen, S., Cooke, R. J., Ramirez-Ruizw, E., et al. 2015, ApJ, 807, 115
Shetrone, M. D., Côté, P., & Sargent, W. L. W. 2001, ApJ, 548, 592
Simon, J. D. 2018, ApJ, 683, 89
Simon, J. D., Li, T. S., Drlica-Wagner, A., et al. 2017, ApJ, 838, 11
Sneden, C., Cowan, J. J., Burris, D. L., & Truran, J. W. 1998, ApJ, 496, 235
Sneden, C., Cowan, J. J., & Gallino, R. 2008, ARA&A, 46, 241
Sneden, C., Cowan, J. J., Lawler, J. E., et al. 2002, ApJL, 566, L25
Sneden, C., Cowan, J. J., Lawler, J. E., et al. 2003, ApJ, 591, 936
Sneden, C., McWilliam, A., Preston, G. W., et al. 1996, ApJ, 467, 819
Sneden, C., Preston, G. W., McWilliam, A., & Searle, L. 1994, ApJL, 431, L27
Tanvir, N. R., Levan, A. J., González-Fernández, C., et al. 2017, ApJL, 848, L27
Torrealba, G., Belokurov, V., Koposov, S. E., et al. 2018, MNRAS, 475, 5085
Tsujimoto, T., Matsuno, T., Aoki, W., Ishigaki, M. N., & Shigeyama, T. 2017, ApJL, 850, L12
Tsujimoto, T., & Nishimura, N. 2015, ApJL, 811, L10
van den Bosch, F. C., Jiang, F., Campbell, D., & Behroozi, P. 2016, MNRAS, 455, 158
van der Walt, S., Colbert, S. C., & Varoquaux, G. 2011, CSE, 13, 22
Vasiliev, E. 2018, arXiv:1802.08239
Venn, K. A., Irwin, M., Shetrone, M. D., et al. 2004, AJ, 128, 1177
Walker, M. G., Mateo, M., Olszewski, E. W., et al. 2015, ApJ, 808, 108
Walker, M. G., Mateo, M., Olszewski, E. W., et al. 2016, ApJ, 819, 53
Wallner, A., Faestermann, T., Feige, J., et al. 2015, NatCo, 6, 5956
Ward, J. H. 1963, J. Am. Stat. Assoc., 58, 236
Westin, J., Sneden, C., Gustafsson, B., & Cowan, J. J. 2000, ApJ, 530, 783
Wetzel, A. R. 2011, MNRAS, 412, 49